This article has been accepted for publication in Geophysical Journal International ©: 2019 The Authors (Benjamin Lee, Martyn Unsworth, Knútur Árnason, Darcy Cordell) *Published by Oxford University Press on behalf of the Royal Astronomical Society. All rights reserved.*

This article has been published in its final form at:

https://doi.org/10.1093/gji/ggz427

Geophysical Journal International

Geophys. J. Int. (2020) **220,** 541–567
Advance Access publication 2019 October 15
GJI Heat flow and volcanology

doi: 10.1093/gji/ggz427

Imaging the magmatic system beneath the Krafla geothermal field, Iceland: A new 3-D electrical resistivity model from inversion of magnetotelluric data

Benjamin Lee [1], Martyn Unsworth,[1] Knútur Árnason[2] and Darcy Cordell[1]

[1] *Department of Physics, University of Alberta, Edmonton, T6G 2R3, Canada. E-mail: blee3@ualberta.ca*
[2] *ISOR Iceland GeoSurvey, Grensásvegur 9, 108 Reykjavik, Iceland*

Accepted 2019 October 2. Received 2019 August 1; in original form 2019 May 9

SUMMARY

Krafla is an active volcanic field and a high-temperature geothermal system in northeast Iceland. As part of a program to produce more energy from higher temperature wells, the IDDP-1 well was drilled in 2009 to reach supercritical fluid conditions below the Krafla geothermal field. However, drilling ended prematurely when the well unexpectedly encountered rhyolite magma at a depth of 2.1 km. In this paper we re-examine the magnetotelluric (MT) data that were used to model the electrical resistivity structure at Krafla. We present a new 3-D resistivity model that differs from previous inversions due to (1) using the full impedance tensor data and (2) a finely discretized mesh with horizontal cell dimensions of 100 m by 100 m. We obtained similar resistivity models from using two different prior models: a uniform half-space, and a previously published 1-D resistivity model. Our model contains a near-surface resistive layer of unaltered basalt and a low resistivity layer of hydrothermal alteration (C1). A resistive region (R1) at 1 to 2 km depth corresponds to chlorite-epidote alteration minerals that are stable at temperatures of about 220 to 500 °C. A low resistivity feature (C2) coincides with the Hveragil fault system, a zone of increased permeability allowing interaction of aquifer fluids with magmatic fluids and gases. Our model contains a large, low resistivity zone (C3) below the northern half of the Krafla volcanic field that domes upward to a depth of about 1.6 km b.s.l. C3 is partially coincident with reported low *S*-wave velocity zones which could be due to partial melt or aqueous fluids. The low resistivity could also be attributed to dehydration and decomposition of chlorite and epidote that occurs above 500 °C. As opposed to previously published resistivity models, our resistivity model shows that IDDP-1 encountered rhyolite magma near the upper edge of C3, where it intersects C2.

In order to assess the sensitivity of the MT data to melt at the bottom of IDDP-1, we added hypothetical magma bodies with resistivities of 0.1 to 30 Ωm to our resistivity model and compared the synthetic MT data to the original inversion response. We used two methods to compare the MT data fit: (1) the change in r.m.s. misfit and (2) an asymptotic *p*-value obtained from the Kolmogorov–Smirnov (K–S) statistical test on the two sets of data residuals. We determined that the MT data can only detect sills that are unrealistically large (2.25 km^3) with very low resistivities (0.1 or 0.3 Ωm). Smaller magma bodies (0.125 and 1 km^3) were not detected; thus the MT data are not sensitive to small rhyolite magma bodies near the bottom of IDDP-1. Our tests gave similar results when evaluating the changes in r.m.s. misfit and the K–S test *p*-values, but the K–S test is a more objective method than appraising a relative change in r.m.s. misfit. Our resistivity model and resolution tests are consistent with the idea of rhyolite melt forming by re-melting of hydrothermally altered basalt on the edges of a deeper magma body.

Key words: Electrical properties; Magnetotellurics; Physics of magma and magma bodies.

Downloaded from https://academic.oup.com/gji/article/220/1/541/5587733 by guest on 30 March 2022

© The Author(s) 2019. Published by Oxford University Press on behalf of The Royal Astronomical Society.

1 INTRODUCTION

Recent studies have investigated the properties of supercritical geothermal reservoirs which are sometimes found at the base of conventional geothermal reservoirs (Fridleifsson & Elders 2005; Scott *et al.* 2015; Watanabe *et al.* 2017). The supercritical fluids found in these reservoirs contain significantly more heat than the steam used in conventional geothermal plants. Fridleifsson (2003) reported that at the same volumetric flow rate, a geothermal well producing supercritical fluids could generate an order of magnitude more electrical power than a conventional well producing steam. The Iceland Deep Drilling Project (IDDP) is a government-industry consortium that has drilled two wells to reach supercritical fluids beneath two operating geothermal fields: the IDDP-1 well at Krafla in 2009 and the IDDP-2 well at Reykjanes in 2017. Drilling of the IDDP-1 well at Krafla ended prematurely at a vertical depth of 2.1 km when the drill head encountered a layer of rhyolitic melt (Elders *et al.* 2014). Although subsequent flow tests produced superheated steam at 450 °C, the pressure was still subcritical at a depth of 2.1 km. The IDDP-2 well at Reykjanes successfully reached supercritical fluid at a total vertical depth of ∼4.5 km with fluid temperature of 426 °C and a pressure of 34 MPa (Fridleifsson *et al.* 2017).

Prior to the IDDP project, extensive geophysical exploration had taken place at Krafla. An upper crustal magma body at Krafla was first inferred from the shear wave shadows observed by Einarsson (1978). Subsequent studies of seismic refraction (Brandsdóttir *et al.* 1997) and seismic tomography (Arnott & Foulger 1994; Schuler *et al.* 2015) imaged low *P*-wave velocity anomalies but no low *S*-wave anomaly was imaged which would indicate a magma body. Extensive magnetotelluric (MT) exploration has also taken place at Krafla by groups from Moscow State University and Duke University (Onacha 2006). Árnason *et al.* (2008) used a 1-D joint inversion of MT and time domain electromagnetic (TEM) data to obtain a 1-D model of subsurface resistivity. This model imaged an electrically conductive layer in the depth range 2 to 4.5 km depth below the geothermal field that was interpreted as being due to partial melt (Árnason *et al.* 2008). Two vertical peaks of low resistivity extended upwards from the inferred magma body in this model (Fridleifsson *et al.* 2014). IDDP-1 was located between these two peaks with the intention of avoiding regions of partial melt. However 1-D inversion of MT data is an approximation and does not always yield a correct model of the subsurface resistivity. To validate the 1-D models, 3-D inversions of the Krafla MT data set were later implemented by a range of authors. Rosenkjaer *et al.* (2015) compared the resistivity models from three different 3-D inversion algorithms and reported that these models had significant differences despite recovering the same main features. These variations are to be expected due to the different inversion algorithms and the fact that inversions are non-unique and many resistivity models can fit the observed MT data to a given statistical level (e.g. Siripunvaraporn 2012). In order to assess if 3-D MT inversion provides an improved resistivity model, this paper will compare a new 3-D resistivity model to the 1-D resistivity model of Árnason *et al.* (2008).

Despite failing to reach supercritical conditions at Krafla, the drilling of the IDDP-1 well gave the opportunity to address important questions about the presence of magma in the crust at shallow depths and the processes that occur as it crystallizes. Although extensive geophysical exploration had been performed at the Krafla geothermal field, the magma body intersected at a depth of 2.1 km had not been imaged geophysically and the well was originally planned to extend to a depth of 4.5 km. Since MT data are sensitive to the presence of aqueous fluids or interconnected melt, it was a surprise to some that the magma body was not detected prior to drilling.

In this paper, we re-examine the Krafla MT data set by performing a systematic 3-D inversion study. Additional data sets and other constraints can be incorporated into the MT inversion in order to reduce the number of resistivity models that will fit a given MT data set to a specified statistical tolerance. A range of approaches were investigated, including inversions that started from the 1-D resistivity model of Árnason *et al.* (2008), in order to include features that have been corroborated by other geophysical methods and drill cuttings from IDDP-1 (Mortensen *et al.* 2014). In particular three possible reasons for the magma body to go undetected will be investigated in this paper:

(1) The location of the rhyolitic magma beneath a low resistivity clay alteration layer in the geothermal field makes it difficult to be resolved with the MT method;
(2) The rhyolitic magma body intersected by IDDP-1 has a relatively high resistivity and/or is relatively small and does not produce an obvious anomaly in the resistivity model.
(3) The magma body was not detected due to limitations of the 1-D inversion.

A key part of the analysis was to undertake resolution tests to evaluate the sensitivity of the MT data to the size, location and resistivity of the upper crustal magma body. Deeper parts of a resistivity model derived from MT inversion are often less constrained by the data than shallower features. Previous studies have sought to evaluate MT data sensitivity to model features by (1) comparing the calculated data between a preferred resistivity model and an edited model (e.g. Campanyà *et al.* 2018; Piña-Varas *et al.* 2018) or; (2) comparing the data misfit of the preferred resistivity model to the data misfit of the edited resistivity model (e.g. Becken *et al.* 2008; Hill *et al.* 2009; Cordell *et al.* 2018). In the first method, if the difference between the two sets of calculated MT data is greater than the data error, then it is assumed that the measured MT data can distinguish between the two models. If the difference is smaller than the data error, then the measured MT data cannot distinguish between the two models, and either model can be considered plausible. However, this method only compares the model responses with no direct reference to the MT data itself. In the second method, the data misfit summary statistics are compared but this method fails to distinguish between up-biasing and down-biasing. As a result, the two misfit values could be similar (or identical) while the two model responses are significantly different from one another. We improve upon both these approaches by applying the two sample Kolmogorov–Smirnov (K–S) statistical test to compare the two sets of residuals (Massey Jr 1951; Miller & Kahn 1962). This is another way to compare the data fit between two resistivity models, and is more quantitative than simply comparing the overall r.m.s. (root mean square) misfit of the models.

2 KRAFLA VOLCANO AND GEOTHERMAL FIELD

Iceland is located on the mid-Atlantic Ridge between the North American and Eurasian tectonic plates. The tectonic activity and volcanism in Iceland is attributed to the combination of the spreading of the mid-Atlantic Ridge with enhanced melt production that results from interactions of the ridge with a mantle plume (e.g. Wolfe *et al.* 1997; Allen *et al.* 1999; Foulger & Anderson 2005). Several

Downloaded from https://academic.oup.com/gji/article/220/1/541/5587733 by guest on 30 March 2022

studies suggest that there is an anomalous layer with low electrical resistivity, low seismic velocity and high temperature gradient beneath much of Iceland (Flóvenz & Gunnarsson 1991; Flóvenz & Sæmundsson 1993; Bjornsson *et al.* 2005). This layer is less than 10 km deep beneath active rift zones, including the Krafla volcanic field, and 20–25 km deep beneath other parts of Iceland (Bjornsson *et al.* 2005). It has been interpreted as a layer of 5–10 per cent mafic melt that accumulates at the base of the crust (Bjornsson *et al.* 2005). Recent laboratory measurements of electrical resistivity show that rocks containing the alteration minerals chlorite and epidote can decrease in resistivity by more than three orders of magnitude when heated to above 500 °C (Manthilake *et al.* 2016; Nono *et al.* 2018). This large decrease in resistivity is due to the destabilization of chlorite and epidote, resulting in the release of conductive aqueous fluids and the formation of interconnected magnetite. Though the cause of this anomalous layer is still under investigation, it seems to be spatially related to the active rift zones in Iceland.

More detailed geophysical studies have taken place at individual volcanic centres in Iceland, including Krafla. The Krafla volcanic field contains a ∼10 km diameter caldera that has an age of 110 ka and which is bisected by an NNE–SSW trending fissure swarm (Fig. 1). The rim is discontinuous and separated by about 3 km east to west due to the spreading of the North American and European plates (∼1.9 cm yr^{-1}; DeMets *et al.* 1990) and burial over time (Árnason *et al.* 2008). Gravity data show an inner caldera, now buried and filled with hyaloclastites (Árnason *et al.* 2008). The calderas and enclosed fissure swarm represent the Krafla central volcano, the focal area of frequent eruptions. The distribution of volcanic rocks at Krafla is strongly bimodal, with felsic rocks (rhyolites) confined to the central volcano (Gudmundsson 1998; Jónasson 2007). Fissure eruptions in the last 3000 yr with a recurrence time of approximately 100 to 300 yr have filled the central volcano with basaltic lavas and hyaloclastites (Sæmundsson 1991). Two major episodes of basaltic fissure eruptions have occurred in recorded history. The first was the 1724–1729 Mývatn Fires and the most recent was the 1975–1984 Krafla Fires (Sæmundsson 1991). The total horizontal extension in the fissure swarm during the Krafla Fires was about 9 m (Tryggvason 1994). The Krafla central volcano has also produced occasional silicic eruptions in the last ∼100 ka. For example, the outer caldera formation was related to a rhyolite dome and composite welded tuff that erupted 110 ka (Sæmundsson 1991) and the inner caldera was formed after subglacial eruptions outside the older caldera (Árnason *et al.* 2008). The origin of bimodal assemblages of rhyolite and basalt at Krafla and across Iceland is unclear; but recent geochemical studies show that Krafla rhyolites form from re-melt of hydrothermally altered basaltic crust (e.g. Sigmarsson *et al.* 1991; Jónasson 1994; Elders *et al.* 2011). The reheating and re-melting of the crust could occur when basaltic melt ascends below Krafla. Einarsson (1978) found areas of high shear wave attenuation (*S*-wave shadows) below the Krafla volcanic field that were interpreted as a shallow magma body at 3 to 7 km depth. Subsequent seismic tomography studies have shown low *P*-wave velocity anomalies within the caldera, but no low *S*-wave anomaly which would indicate a magma body (e.g. Brandsdóttir *et al.* 1997; Schuler *et al.* 2015; Kim *et al.* 2017).

Krafla is well known for its geothermal field characterized by high temperatures (>200 °C) at shallow depth. Geophysical exploration at Krafla began in the 1970s in order to understand the structure of the underlying geothermal reservoirs. The Krafla geothermal power station began operation in 1977 and has a current capacity of 60 MWe with 19 production wells as of 2015. The Krafla geothermal field is divided into several subfields based on location, thermohydraulic conditions, fluid chemical composition, and isotopic content of the thermal water. In this study we will focus on the subfields within the central caldera: the Leirbotnar, Vitismor, Vesturhlidar, and Sudurhlidar subfields (Fig. 1). In the northern part of Krafla, the Hveragil fault system divides the Vitismor and Leirbotnar fields in the west from the Sudurhlidar field to the east. Vesturhlidar is located in the northern part of Hveragil, east of the Viti crater. The Hveragil fault system appears to be a boundary between distinct thermal conditions and alteration to the east and west. The chlorite–epidote zone is relatively shallow beneath Sudurhlidar (0.2–0.3 km a.s.l.), whereas it is 0.2 to 0.3 km b.s.l. beneath Leirbotnar and Vitismor. Temperatures beneath Sudurhlidar and Vesturhlidar at shallow depths (above 0.4 km b.s.l.) are generally higher than those in Leirbotnar and Vitismor (Weisenberger *et al.* 2015). Temperatures are high enough for a two-phase system beneath Sudurhlidar and Vesturhlidar at shallow depths (∼0.2 km b.s.l.) However, beneath Leirbotnar and Vitismor there are two distinct reservoirs: a shallow, almost isothermal (∼200 °C) liquid reservoir above ∼0.5 km b.s.l., and a deeper two-phase reservoir. Chlorite–epidote alteration in the upper reservoir indicates that a two-phase system existed there in the past. Data from over 40 wells have contributed to the understanding of this complex geothermal field.

Supercritical fluids may exist at the base of geothermal systems such as Krafla. The Iceland Deep Drilling Project (IDDP) group considered searching for supercritical fluids beneath Krafla partly due to the high temperatures (>300 °C) encountered at relatively shallow depth (2 km) (Fridleifsson 2003; Fridleifsson & Elders 2005). The IDDP group drilled the exploratory IDDP-1 well in 2009 with the goal of reaching supercritical fluids approximately 4 km below the Krafla geothermal field. However, drilling was prematurely stopped when a layer of rhyolitic magma was encountered at 2.1 km depth (Fridleifsson *et al.* 2014). The bottom-hole temperature was estimated to be as high as 500 °C, corresponding to a superheated reservoir. The recovered cuttings consisted of basaltic lavas and hyaloclastites to a depth of 1.36 km, an intrusive complex of basaltic dykes and dolerite from 1.36 to 2 km depth, and granophyres and felsites below 2 km (Mortenson *et al.* 2014).

Prior to drilling IDDP-1, magma was not expected to be found at such a shallow depth, although it was considered a possibility after the nearby well K-39 intersected rhyolitic magma at a total vertical depth of about 2.6 km (Mortensen *et al.* 2010). Previous 1-D modelling of magnetotelluric (MT) data predicted a low resistivity zone at about 4.5 km depth below Krafla, interpreted as partial melt or aqueous fluids (Árnason *et al.* 2008; Fridleifsson *et al.* 2014). It is important to investigate why the 1-D MT modelling did not predict the presence of magma at 2.1 km below Krafla. In the following sections we will use a different approach than previously published work (Árnason *et al.* 2008; Gasperikova *et al.* 2015; Rosenkjaer *et al.* 2015) to model and analyse the Krafla MT data.

3 MAGNETOTELLURIC DATA AT KRAFLA

Electrical resistivity (DC) and electromagnetic (EM) methods such as the time domain electromagnetic method (TEM) and magnetotellurics (MT) are used to map variations in electrical resistivity. MT is distinct from other EM methods because it is able to measure signals in a broad frequency range of the EM spectrum (∼10^{4}–10^{-5} Hz). Because exploration depth depends on frequency, audio (high) frequency MT equipment is suitable for shallow surveys, and

Downloaded from https://academic.oup.com/gji/article/220/1/541/5587733 by guest on 30 March 2022

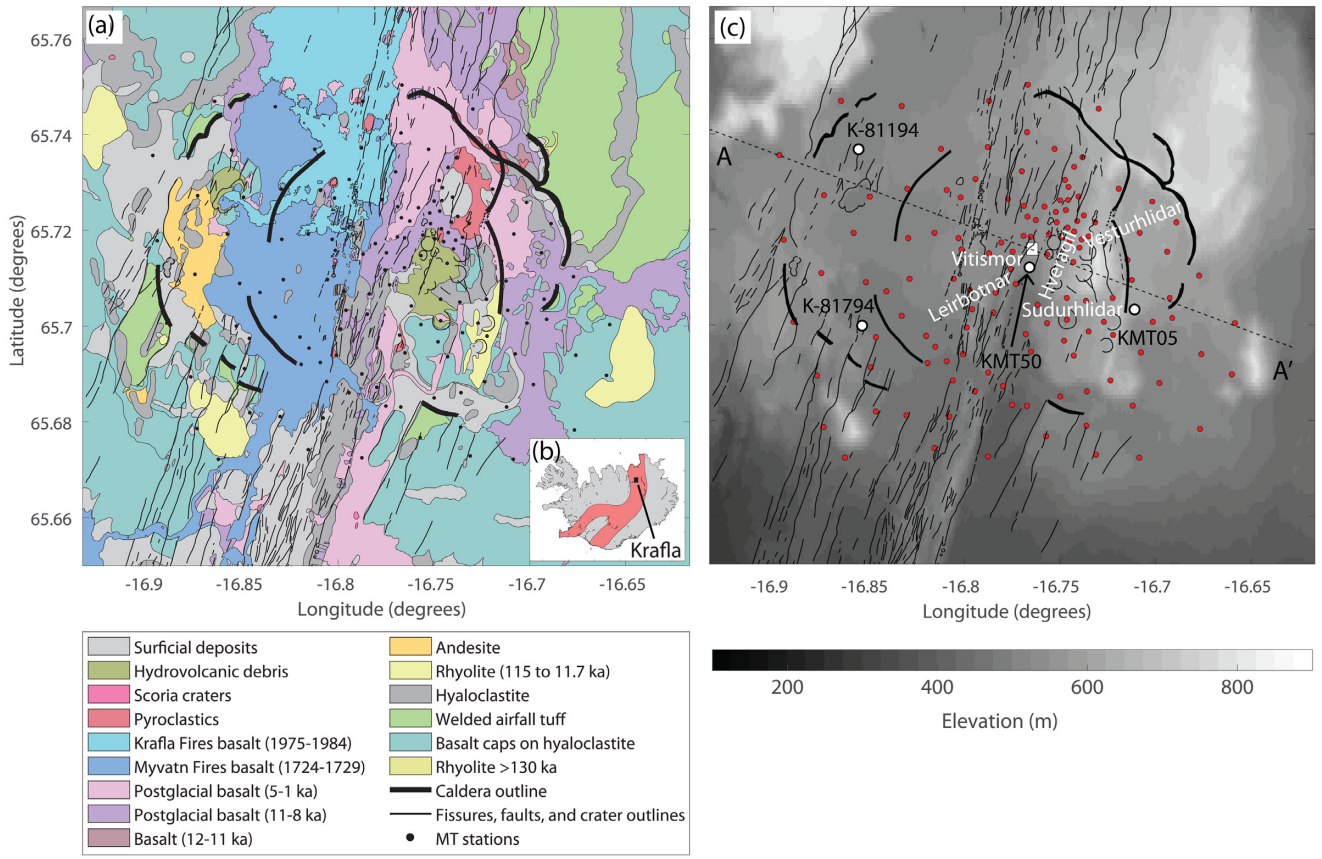

Figure 1. (a) Geological map of the Krafla volcanic field; (b) location of Krafla with the neo-volcanic zone of Iceland shaded in red. (c) Topographic map of the Krafla volcanic field with labelled geothermal fields. The thick black lines show fissures and the caldera rims. The outer caldera formed about 110 ka and is ∼10 km in diameter, while the inner caldera formed about 80 ka and is filled with hyaloclastites. The red circles are locations of MT stations, and the white square is the location of the IDDP-1 well. The white circles are MT stations mentioned in the text. A–A' is the profile shown in Fig. 9.

long period (low frequency) MT is suitable for deeper exploration. Broad-band MT equipment measures signals in the intermediate frequencies and can be used effectively in both cases. MT is particularly useful in volcano and geothermal studies because it can detect resistivity variations due to water content, low temperature (<220 °C) alteration and partial melt that typically have a low resistivity compared to the host rock (e.g. Bibby *et al.* 2009; Árnason *et al.* 2010; Cumming & Mackie 2010). The MT method measures naturally occurring EM signals to image the electrical resistivity of the Earth. High frequency signals (>1 Hz) originate from worldwide lightning storms, and low-frequency signals (<1 Hz) are derived from interactions of the solar wind with the Earth's magnetosphere. When an EM wave reaches the surface of the Earth, it is refracted vertically downwards, diffuses into the ground and decays as a function of the signal frequency f and the resistivity of the Earth (ρ). A proxy for the depth of investigation is given by

$$\delta \approx 503\sqrt{\frac{\rho}{f}} \tag{1}$$

,where δ is the so-called skin depth in metres, ρ is the Earth resistivity in Ωm, and f is signal frequency in Hz. Each MT station records time-series with five channels of data: two orthogonal electric field components (E_x, E_y) and three orthogonal magnetic field components (H_x, H_y, H_z), where the x, y, and z directions are geographic north, geographic east and vertically downwards, respectively. The Fourier transformed horizontal components of the electric and magnetic fields are used to calculate the impedance tensor, Z as a function of frequency or period which is defined as:

$$\begin{bmatrix} E_x \\ E_y \end{bmatrix} = \begin{bmatrix} Z_{xx} & Z_{xy} \\ Z_{yx} & Z_{yy} \end{bmatrix} \begin{bmatrix} H_x \\ H_y \end{bmatrix}. \tag{2}$$

The impedance contains information about the spatial distribution of electrical resistivity in the Earth. In the 3-D case the electrical resistivity varies in the x, y, z directions and the four components of the impedance tensor are non-zero. The complex impedance tensor is commonly expressed in terms of apparent resistivity and phase angle. The apparent resistivity, ρ_{ij}, is calculated with:

$$\rho_{ij} = \frac{|Z_{ij}|^2}{2\pi f \mu_0}, \tag{3}$$

where μ_0 is the magnetic permeability of free space, and i, j are the components of the impedance tensor, Z. Apparent resistivity is a volume-averaged resistivity in Ωm; the lower the frequency, the greater the depth that is sampled. The phase, φ_{ij}, is defined as

$$\varphi_{ij} = \tan^{-1}\left[\frac{Im\left(Z_{ij}\right)}{Re\left(Z_{ij}\right)}\right], \tag{4}$$

where $Im(Z_{ij})$ and $Re(Z_{ij})$ are the imaginary and real parts of Z_{ij}, respectively. The phase angle is commonly expressed in the first quadrant ($0^\circ \leq \varphi \leq 90^\circ$) such that it indicates whether apparent resistivity increases ($\varphi_{ij} < 45^\circ$) or decreases ($\varphi_{ij} > 45^\circ$) as frequency decreases. Apparent resistivity and phase, when viewed over a range

Downloaded from https://academic.oup.com/gji/article/220/1/541/5587733 by guest on 30 March 2022

of frequencies, are useful to study resistivity changes due to changes in geology and rock properties.

Vertical magnetic field transfer function (tipper) data relate the vertical magnetic field H_z to the two horizontal magnetic field components. Tipper data contain information about spatial resistivity variations but electric field data are needed to constrain absolute resistivity values. These tipper data provide complementary information to the impedance data, but were not used in this study due to the reasons discussed below.

A total of 163 MT stations were collected at the Krafla volcanic field during campaigns conducted by Duke University (2004–2005) and Moscow State University and Iceland GeoSurvey (ÍSOR; 2006 and 2008). The data consist of broad-band MT soundings in the frequency ranges of 320–0.001 Hz. Time domain electromagnetic (TEM) data were also collected to correct galvanic distortion caused by localized, near-surface resistivity anomalies. We used 133 of the original 163 MT stations in our 3-D inversion due to practical considerations that will be described in detail in the next section. The selected stations are shown in Fig. 1. Tipper data were available for 35 out of the 133 selected MT stations. However, we did not include these data in our inversion because many of these stations had significant noise in the tipper in the 10–0.001 Hz range. Although we do not have access to the MT time-series data, we believe that signals from the nearby Krafla power plant infrastructure may have contaminated the vertical magnetic field data. In future work it may be useful to reprocess the tipper data because they provide information on lateral resistivity variations.

Prior to inverting the data, it is useful to analyse qualitative trends in the measured MT data. Figs 2–5 show a map view of the apparent resistivity and phase data (xy component, yx component and computed from determinant of impedance) over a range of frequencies. In Fig. 2 data at 40 Hz is shown, and at this high frequency, the data are sensitive to the near-surface (<1 km) resistivity structure of the Krafla volcanic field. Areas with low apparent resistivity correspond to the shallow clay layer (smectite/zeolite), and areas with higher apparent resistivity (>100 Ωm) correspond to basalt and hyaloclastites (e.g. Árnason *et al.* 2000). At 40 Hz most of the phase data outside of the clay layer is greater than 45°, corresponding to a decrease in apparent resistivity with depth as the data begin to image structure below the resistive surface basalt.

Fig. 3 shows the same quantities at a frequency of 0.3 Hz. Data at this frequency have similar spatial variations as in Fig. 2; however, the phases are lower which indicates that resistivity is no longer decreasing as a function of (decreasing) frequency (increasing period). At frequencies of 40 and 0.3 Hz the outline of the inner caldera appears as an abrupt resistivity contrast. Low resistivity inside the inner caldera corresponds to subglacial hyaloclastite, and high resistivity outside the inner caldera corresponds to basaltic lava filling in the outer caldera.

Fig. 4 shows a map view of the apparent resistivity and phase data at a frequency of 0.037 Hz, which corresponds to the upper few kilometres below the volcanic field. At 0.037 Hz the low apparent resistivity beneath the shallow clay cap is likely associated with a magmatic heat source and/or elevated concentrations of aqueous fluids. The high apparent resistivity within the geothermal field inside the inner caldera corresponds to chlorite–epidote alteration minerals stable at 220 to 500 °C. The phase data are mostly greater than 45°, indicating that the apparent resistivity is decreasing with depth.

Fig. 5 shows the apparent resistivity and phase for a frequency of 0.0092 Hz which show a deep conductor below Krafla. Most stations have a low apparent resistivity and phase greater than 45° at this frequency. This may correspond to the regional conductor beneath Iceland observed by Bjornsson *et al.* (2005).

Fig. 6 shows examples of apparent resistivity and phase curves for four stations at Krafla (see Fig. 1 for station locations). Stations K-81194 and K-81794 are located in the outer caldera in the west part of the Krafla volcanic field. These two stations exhibit similar apparent resistivity and phase curves. At high frequencies the slightly decreasing apparent resistivity indicates shallow moderately low resistivity. 1-D inversion of TEM data (Árnason *et al.* 2008) shows much higher resistivity in this area than inside the inner caldera. Stations KMT05 and KMT50 are located on the eastern and central parts of the calderas, respectively. These stations exhibit a more dramatic decrease in apparent resistivity at high frequencies, corresponding to a thicker clay layer. At intermediate frequencies, all four stations increase in apparent resistivity with decreasing frequency as the data are sensitive to the resistive chlorite–epidote alteration products. At low frequencies the data show a decrease in apparent resistivity which may be a deeper magma body or regional conductor beneath Krafla.

The phase tensor, which is independent of local distortions of the electric field, is also a useful tool in evaluating MT data because it can estimate the data dimensionality and direction of the geoelectric strike (Caldwell *et al.* 2004). The minimum phase tensor value, maximum phase tensor value and skew angle are three coordinate invariants of the phase tensor that can be represented as a coloured ellipse. When shown in map view, a predominant geoelectric strike direction can be inferred from the elongated ellipses that align to the preferred flow direction of electric current. The skew angle (β) represents the asymmetry of the phase tensor due to a 3-D resistivity distribution. Large skew angles are indicative of a 3-D resistivity distribution; however, small skew angles do not necessarily preclude one (Booker 2014). Here we show maps of phase tensors to help understand the directionality and dimensionality of resistivity structures at Krafla. Fig. 7 shows a map view of phase tensor ellipses at four frequencies. For each frequency, each station is represented by a coloured ellipse. The ellipse axes are proportional to the maximum and minimum values of the phase tensor, and the colour indicates the absolute value of the skew angle. Note that the size of each ellipse is normalized by its maximum phase tensor value. A polar histogram that shows the major axis direction for each station is also shown for each frequency. At 40 Hz the data at each station are sensitive only to near surface structure and there is some variation in strike direction from station to station. However, many stations have a strike direction of approximately N20° E at this frequency, which agrees with the direction of the fissure swarm. At a frequency of 0.3 Hz there is no clear predominant strike direction, and many stations have a skew angle greater than 3° which is indicative of 3-D resistivity structures at this frequency. At frequencies of 0.037 and 0.0092 Hz the alignment of the ellipses with the NNE–SSW direction of the fissure swarm and low skew angles suggest that the MT data are relatively 2-D at lower frequencies. Note that in the 2-D case the phase tensor major axes are aligned either parallel or perpendicular to the strike direction. At low frequencies, the phase tensor major axes align in the direction of the rifting at Krafla because the phase data begin to detect a resistive feature beneath the deep conductor (e.g. station data curves in Fig. 6). Overall the phase tensors and apparent resistivity indicate a relatively complicated resistivity structure beneath Krafla that requires a 3-D approach to model the 3-D resistivity structure at intermediate frequencies.

As described in the previous section, Árnason *et al.* (2008) performed joint 1-D TEM–MT inversions on 125 MT stations that were corrected by nearby TEM soundings and presented the

Downloaded from https://academic.oup.com/gji/article/220/1/541/5587733 by guest on 30 March 2022

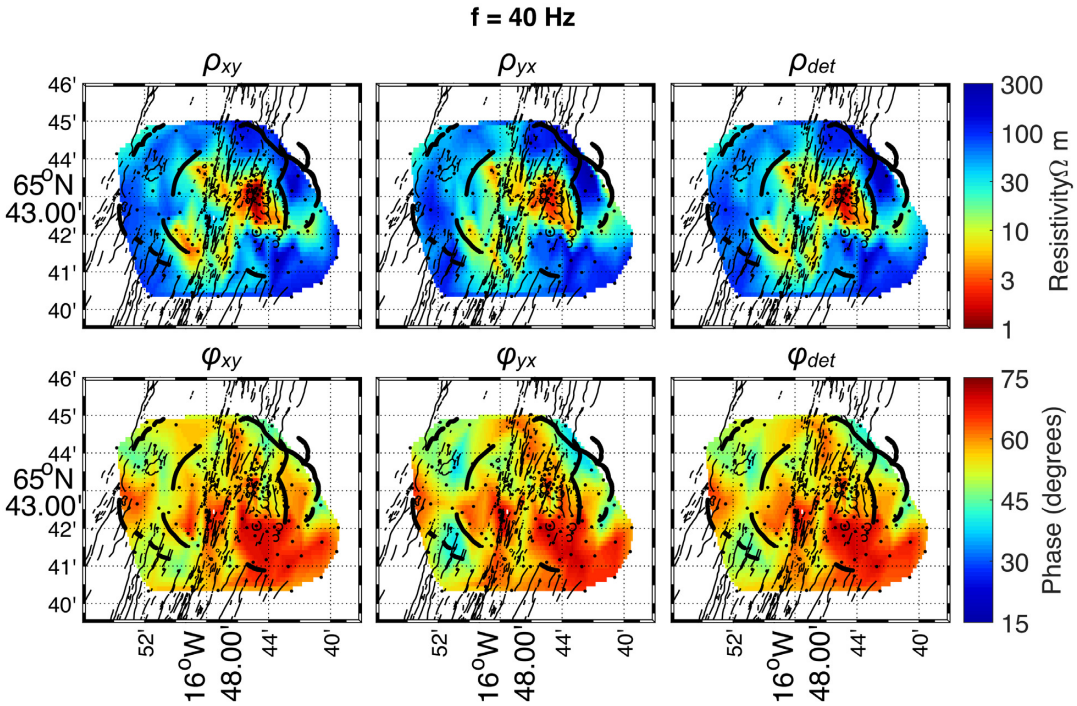

Figure 2. Map view of the Krafla MT apparent resistivity (ρ) and phase (φ) data at a frequency of 40 Hz. xy = electric field oriented geographic north and magnetic field oriented geographic east; yx = electric field oriented geographic east and magnetic field oriented geographic north; det = quantity derived from determinant of MT impedance data. These data are sensitive to the near-surface (<1 km) and reveal lateral variations in resistivity in the Krafla volcanic field. The apparent resistivity data show low resistivity areas that correspond to the shallow clay layer (smectite/zeolite) and high apparent resistivity (>100 Ωm) areas of near-surface basalt and hyaloclastites. The phase data show a more complicated pattern; but the phase across most of the volcanic field is greater than 45°, corresponding to a decrease in resistivity as the data begin to probe the underlying geothermal reservoirs. Thick black lines = outline of inner and outer caldera; thin black lines = fissures and craters; filled black circles = MT stations with data at this frequency; open circles = MT stations with no data at this frequency.

resulting resistivity model as interpolated horizontal and vertical cross-sections. In this paper we show selected slices through the interpolated 1-D resistivity model in Figs 9 and 10. A 1-D inversion only accounts for resistivity variations with depth at each MT station and may be inaccurate in more complex geological settings. A 3-D inversion does not require any assumptions about the subsurface resistivity distribution. However, in consideration of the large amount of data and model parameters, along with numerous settings that control the inversion algorithm, some care is required in order to obtain a satisfactory result (e.g. Siripunvaraporn 2012; Miensopust 2017). In practice, a different resistivity model can be obtained from the inversion simply by choice of data frequencies or size of the cells in the model, among other parameters. Many inversion settings and parameters should be tested to understand the consistency and reliability of the inversion results. In the case of the Krafla MT data set, Gasperikova *et al.* (2015) and Rosenkjaer *et al.* (2015) presented resistivity models obtained from three 3-D inversion algorithms. The three models contained the same main features but had significant differences. The main features of the resistivity models are:

(1) At shallow depths (<2 km below surface) resistivity values agree well with the expected alteration mineralogy. High resistivity values (>1000 Ωm) are correlated with unaltered basalt that fills the Krafla outer caldera and low resistivity values in the inner caldera are associated with a shallow clay layer.

(2) Smectite alteration occurs in the temperature range 100 to 220 °C and results in a low resistivity (<10 Ωm) clay layer in the upper 500 m.

(3) At the base of the clay layer, relatively resistive (100–1000 Ωm) chlorite and epidote alteration minerals are stable at temperatures of 220 to 500 °C.

(4) A conductive (<10 Ωm) domed feature at a depth of ∼2.5 km beneath the Krafla caldera was interpreted as a magma body/intrusion.

4 NEW APPROACH TO THE KRAFLA 3-D MAGNETOTELLURIC INVERSION

Unlike 1-D and 2-D MT inversion algorithms, 3-D inversion algorithms do not require assumptions about the dimensionality of the Earth's electrical resistivity. 1-D and 2-D inversions are computationally inexpensive and provide valuable information, but may not be appropriate for complex geological settings. Apparent resistivity and analysis of phase tensors in the previous sections suggest that a 3-D inversion is appropriate for the Krafla MT data set.

Our first step in the process of inverting the MT data was to select a subset of the data for inversion. Ideally, the inversion needs a set of MT stations that are uniformly distributed on the surface and that sample the entire area of interest. In model discretization there should not be more than one MT station in each model cell, and there should be a few model cells between each pair of MT stations. This ensures that the inversion is able to place resistivity variations between stations, particularly when there are small, near-surface features. Because the computational cost of an inversion depends on the number of model cells, there is a trade-off between including more data/model cells and incurring a higher computational cost.

Downloaded from https://academic.oup.com/gji/article/220/1/541/5587733 by guest on 30 March 2022

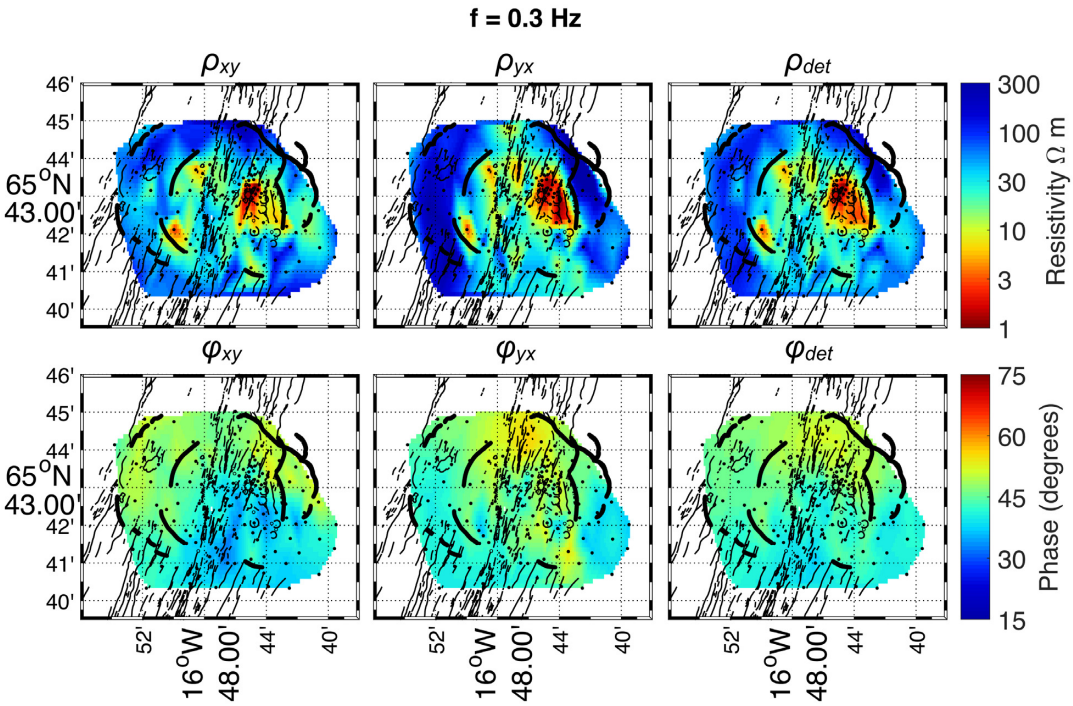

Figure 3. Map view of the Krafla MT apparent resistivity (ρ) and phase (φ) data at a frequency of 0.3 Hz. xy = electric field oriented geographic north and magnetic field oriented geographic east; yx = electric field oriented geographic east and magnetic field oriented geographic north; det = quantity derived from determinant of MT impedance data. Data at this frequency has similar spatial variations as in Fig. 2; however the phases are lower which indicates that resistivity is no longer decreasing as a function of frequency. The inner caldera outline separates low resistivity in the subglacial hyaloclastite fill from high resistivity basaltic subaerial lavas in the outer caldera. Thick black lines = outline of inner and outer caldera; thin black lines = fissures and craters; filled black circles = MT stations with data at this frequency; open circles = MT stations with no data at this frequency.

At Krafla the distance between neighbouring MT stations ranges from 100 m to more than 1 km. In the case of two stations that were less than about 300 m apart, we excluded the station with lower quality MT data in order to remove redundant data and to minimize the number of model cells. Our model mesh includes topography and contains 119 cells in the north–south direction, 142 in the east–west direction and 84 in the vertical direction. Layers above sea level have a thickness of 40 m, and the first layer beneath sea level has a thickness of 30 m that increases by a factor of 1.1 for each subsequent layer. The core mesh contains 100 m by 100 m horizontal cells to allow room for multiple model cells between each station.

In addition to spatial sampling, data frequency selection is an important step prior to the inversion. We selected 19 frequencies, logarithmically spaced, from 320 to 0.00114 Hz. The highest and lowest frequencies determine the smallest and largest resolvable depths, respectively. For example, following eq. (1), in a 10 Ωm half-space the highest frequency of 320 Hz will penetrate about 90 m into the subsurface, and the lowest frequency of 0.00114 Hz will sample to a depth of 46 km. We included 19 frequencies in order to accurately represent the smooth variations of impedance as a function of frequency.

Each datum in the inversion must be assigned an error (uncertainty) estimate. This value is important as the inversion seeks a solution to minimize the misfit of each datum. Large error estimates may cause the inversion to inadequately fit the measured data; error estimates that are too small may cause noise to be fit and result in a rough model. The standard impedance errors obtained from time-series processing may be very small compared to the impedance values (<1 per cent) and it may be necessary to apply an error floor in order to obtain a satisfactory inversion result. In our inversion we applied an error floor equal to 5 per cent of $\sqrt{|Z_{xy}Z_{yx}|}$.

It is important to consider the effects of galvanic distortion on the measured MT data. Galvanic distortion is caused by local distortions of electrical current from either (1) near-surface features smaller than the resolvable limit of the MT data, or (2) extreme topographic relief. Several methods to determine galvanic distortion in the electric field define a 2 × 2, frequency-independent distortion tensor (e.g. Bahr 1988; Groom & Bailey 1989). The Groom & Bailey (1989) tensor decomposition method factors the distortion tensor into four components: (1) the twist and (2) shear tensors that modify impedance amplitudes and phases, (3) the anisotropy tensor that modifies amplitudes and (4) the scalar gain that modifies amplitudes. When the Earth has a 2-D regional geologic strike and 3-D distorting bodies, the twist and shear tensors can be solved but anisotropy and gain (together commonly called 'static shift') cannot be uniquely determined. In a 3-D Earth where all elements of the impedance tensor are significant, different approaches must be used. There has been some debate about how to handle galvanic distortion in the 3-D inversion of MT data (Miensopust 2017). The unknown scalar shifts at each MT station can be solved by jointly inverting MT and TEM data (e.g. Árnason *et al.* 2010). Alternatively, the distortion tensor can be simultaneously inverted with the MT impedance (e.g. Sasaki & Meju 2006; Avdeeva *et al.* 2015; Usui *et al.* 2016). Even if distortion is not explicitly handled in the inversion, Patro & Egbert (2011) found that for moderately distorted data (e.g. no out-of-quadrant phases or mode splits of several orders of magnitude) the 3-D inversion placed small, near-surface features into the model to accurately reproduce distortion in the MT data. We

Downloaded from https://academic.oup.com/gji/article/220/1/541/5587733 by guest on 30 March 2022

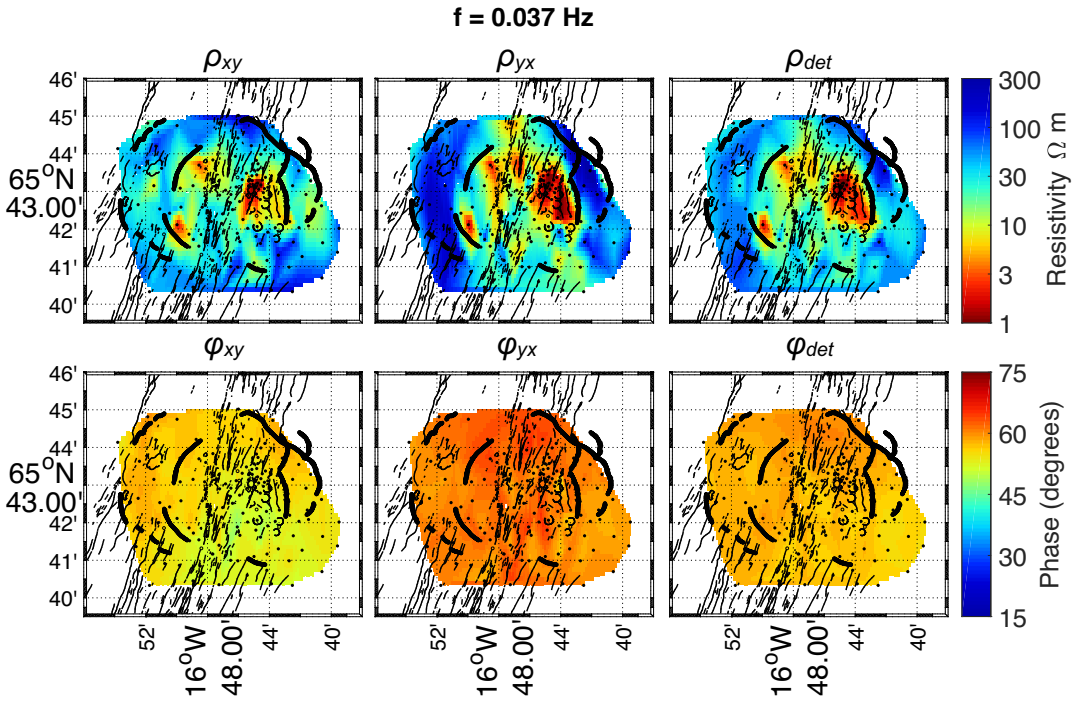

Figure 4. Map view of the Krafla MT apparent resistivity (ρ) and phase (φ) data at a frequency of 0.037 Hz. xy = electric field oriented geographic north and magnetic field oriented geographic east; yx = electric field oriented geographic east and magnetic field oriented geographic north; det = quantity derived from determinant of MT impedance data. These data are sensitive to the upper few km below the Krafla volcanic field. The apparent resistivity data show a low resistivity feature beneath the east part of the inner caldera and a high resistivity beneath the middle of the inner caldera. The phase data are mostly greater than 45°, indicating that the apparent resistivity is decreasing with depth as most MT stations begin to detect a conductor at the root of the geothermal system. Thick black lines = outline of inner and outer caldera; thin black lines = fissures and craters; filled black circles = MT stations with data at this frequency; open circles = MT stations with no data at this frequency.

chose to implicitly allow distortion in our model by designing our mesh to contain 2 to 3 small (100 m by 100 m) cells between each MT station. These small cells allow the inversion to place small, distorting features into the resistivity model.

A number of inversions were undertaken to determine the optimal regularization parameters, starting model and prior model. The ModEM 3-D inversion algorithm that we used contains a model covariance matrix that controls the change in resistivity (spatial smoothing) between neighbouring model cells (Kelbert *et al.* 2014). This allows the user to specify the smoothing constraints in three spatial directions. We varied the degree of smoothing in test inversions, but in every inversion we applied the same model covariance length scale value in each spatial direction. The ModEM algorithm attempts to minimize differences in resistivity between the recovered model and the prior model. In this section we test if the recovered resistivity model is dependent on our choice of prior models with two representative inversions:

(1) A uniform starting and prior model
(2) A uniform starting model with interpolated 1-D prior model.

4.1 Uniform starting and prior model

This inversion used a 10 Ωm half-space starting and prior model. We tested other resistivity values and found that the inversion with the 10 Ωm half-space resulted in good data fit and a model with reasonable structure at all depths. We used the ModEM code of Kelbert *et al.* (2014) to invert the full impedance tensor (eight components). After 98 iterations the inversion converged to an overall r.m.s. misfit of 1.04. Fig. 6 shows the measured and calculated data for four selected stations (see Fig. 1). The data fit was relatively uniform for all stations and frequencies with no significant outliers (see Fig. 8). In particular, the low r.m.s. misfit at high frequencies suggests that the inversion adequately fit the MT data with static shifts. Figs 9 and 10 show selected slices through the resistivity model; we will discuss model interpretation in the next section.

We performed different inversions to test whether or not the main resistivity features in the model were strongly dependent on the inversion settings. If the resistivity and spatial extent of a model feature greatly varies from changing one setting, then it may not be well-constrained by the MT data. In these tests we considered the inversion that used a 10 Ωm half-space starting and prior model. We tried changing the model covariance setting to see if any model features would significantly change. Fig. A1 shows the diagonal slice A–A' through the unconstrained inversion resistivity models with covariance length scale values of 0.1, 0.3 and 0.5. Because the model covariance values control the smoothing between neighbouring model cells, the effect of changing covariance values depends on the size of cells in the mesh. Slezak *et al.* (2019) tested multiple covariance length scale values in their ModEM MT inversions and found that values that were too small resulted in resistivity models that only contained heterogeneities near the surface. We observed a similar effect in the Krafla MT inversion, where the resistivity model obtained from a covariance value of 0.1 did not contain much detail at greater depth. It is clear from Fig. A1 that the covariance setting of 0.1 is not within the optimal range for our data and mesh. Thus, it is important to test a range of model covariance values to find

Downloaded from https://academic.oup.com/gji/article/220/1/541/5587733 by guest on 30 March 2022

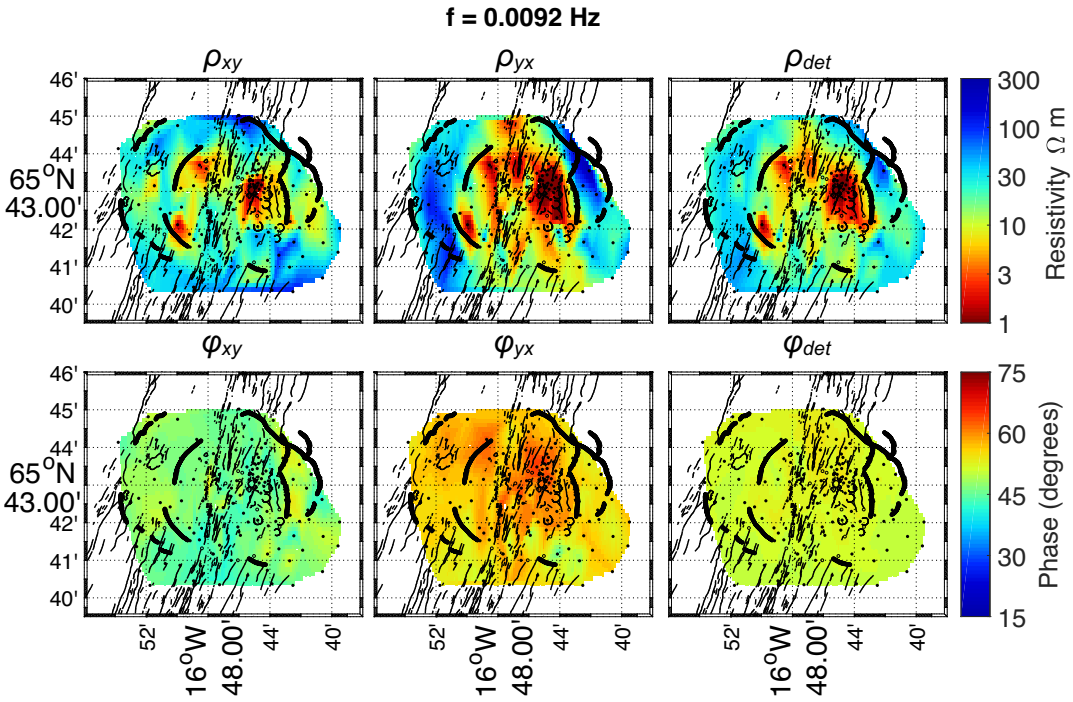

Figure 5. Map view of the Krafla MT apparent resistivity (ρ) and phase (φ) data at a frequency of 0.0092 Hz. xy = electric field oriented geographic north and magnetic field oriented geographic east; yx = electric field oriented geographic east and magnetic field oriented geographic north; det = quantity derived from determinant of MT impedance data. Most stations have a low apparent resistivity and phase greater than 45°. This may correspond to the deep regional conductor beneath Iceland observed by Bjornsson et al. (2005). Thick black lines = outline of inner and outer caldera; thin black lines = fissures and craters; filled black circles = MT stations with data at this frequency; open circles = MT stations with no data at this frequency.

an optimal value for a particular set of data and mesh. The optimal model covariance (smoothing) parameter was set to 0.3 in each direction (x, y and z) and used for all inversions.

4.2 Uniform starting model with 1-D prior model constraint

The inversion of MT data is inherently non-unique. By changing the inversion parameters and regularization, a broad range of models can be obtained that all fit the measured data. In the absence of any *a priori* geological information, the resulting 3-D resistivity model can also be influenced by the choice of the starting model. For example, if a half-space of constant resistivity is chosen as the starting model to emphasize model smoothness, the inversion is free to fit the observed MT data with resistivity structure that may not be geologically reasonable. In the case of Krafla, there is a significant amount of geophysical and geological information that can help to constrain the 3-D MT inversion towards a more reasonable result. Gravity, shear wave attenuation, seismic tomography and MT studies at Krafla have all given evidence for a magma body located at about 3 km depth beneath the Krafla central volcano. The presence of the magma body is confirmed by several methods and can be included as *a priori* information in the 3-D MT inversion. We chose to incorporate the deep magma body and other features such as the shallow clay layer, in the form of the 1-D MT models presented by Árnason *et al.* (2008). Although few geological environments can truly be considered 1-D, the 1-D analysis provides information about how resistivity varies with depth. We interpolated the 125 1-D resistivity models onto a 3-D mesh to create a prior model for the 3-D MT inversions. A slice through the prior model is shown in Fig. 9. The misfit between the observed MT data and the 3-D data calculated from the interpolated 1-D MT model is 7.55. Clearly the interpolated 1-D model will not fit the data when considering three spatial dimensions. However, the 1-D prior model can be a useful constraint by limiting deviations in the model from known structures such as the shallow clay layer and deeper conductor.

Apart from the change in prior model, the inversion used identical parameters to the unconstrained inversion discussed in Section 4.1. The r.m.s. misfit between the observed and calculated data converged to a value of 1.05. Even with the interpolated 1-D model as the prior model, the constrained inversion recovered a very similar model to the unconstrained inversion. The differences between the two models will be discussed in the next section.

5 RESISTIVITY MODEL INTERPRETATION

The unconstrained and constrained inversion models in Figs 9 and 10 contain similar features, which are summarized below.

5.1 Model features

Shallow low resistivity layer (C1)

The low resistivity layer C1 is a prominent feature in the two inversion models. Clay minerals such as smectite are common low-temperature (100 to 220 °C) hydrothermal alteration products and are the cause of the low resistivity of this feature. Smectite has a very high cation exchange capacity (CEC) and as a result, a low resistivity. The smectite zone (or smectite/chlorite mixed layer) in

Downloaded from https://academic.oup.com/gji/article/220/1/541/5587733 by guest on 30 March 2022

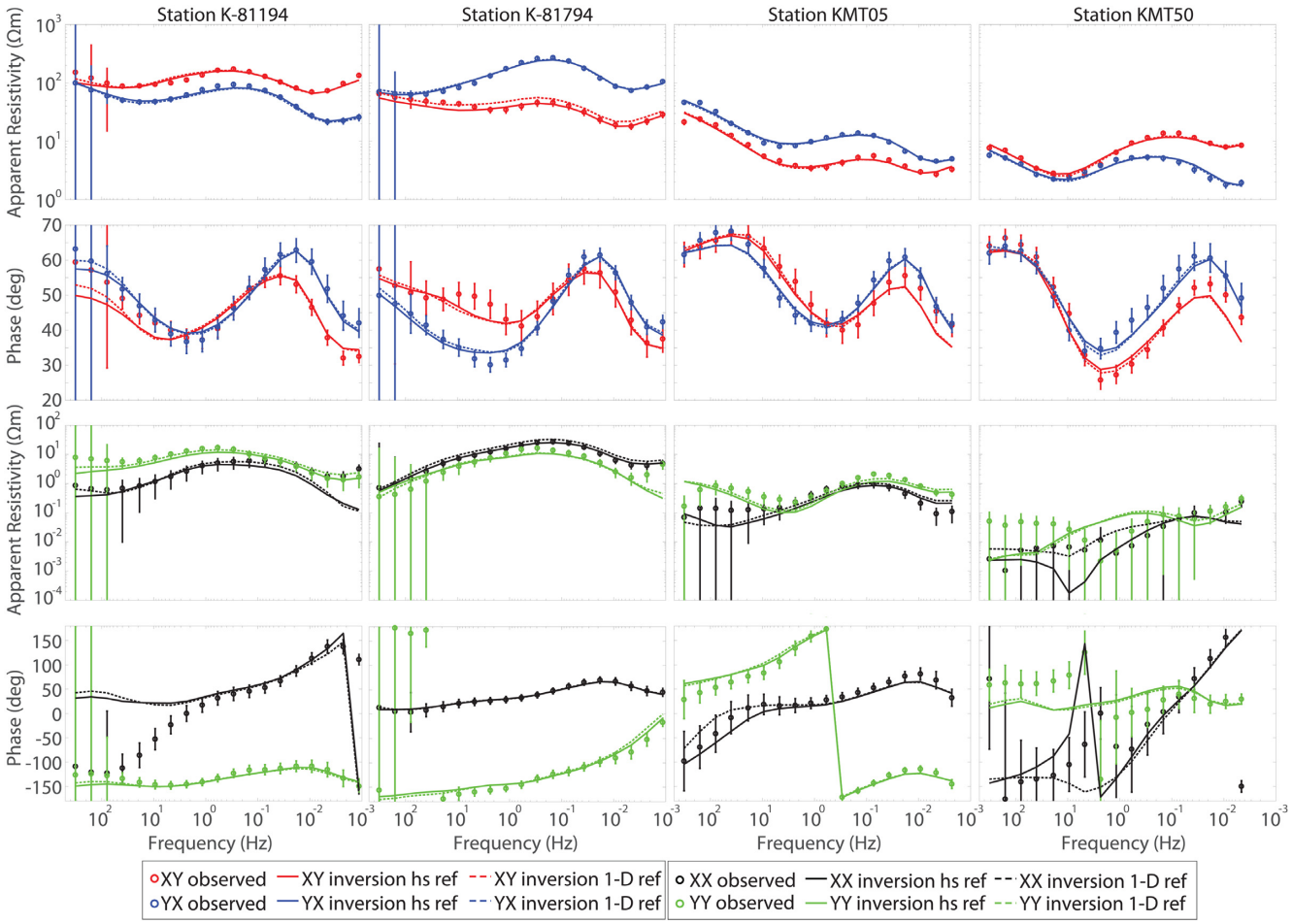

Figure 6. Selected apparent resistivity and phase curves from stations K-81 194, K-81 794, KMT05, and KMT50. See Fig. 1 for station locations. The symbols with error bars are the measured MT data and the solid lines represent the unconstrained inversion response. Red = xy mode data; blue = yx mode data; black = xx mode data; green = yy mode data.

our model appears as a low resistivity layer that extends to a depth of about 0.3 km a.s.l., which is coincident with the depth where chlorite was first observed in the IDDP-1 log (Mortensen *et al.* 2014).

Due to the diffusive nature of the EM signals measured by MT, there is non-uniqueness in resolving multiple low-resistivity layers (Simpson & Bahr 2005). In our model, C1 could prevent the detection of deeper features because it is a low resistivity clay layer with a thickness of a few hundred metres and a resistivity of 1–10 Ωm. We can estimate the integrated conductivity (i.e. conductance) of C1 to find the minimum conductance a deeper conductor would need in order to be resolved. Fig. 11 shows the conductance from the surface of the model to an elevation of 0.2 km b.s.l. (about 0.6 km beneath the IDDP-1 well pad). The conductance map shows a high conductance (>300 S) within the inner caldera that coincides with the conductive clay layer. The conductance varies laterally because C1 does not have a uniform thickness. From this map we can estimate that a deeper low resistivity feature needs a conductance greater than 300 S to be resolved in the resistivity model.

High-temperature reservoir/chlorite–epidote alteration zone (R1)

This feature extends from a depth of about 0.1 to 1 km b.s.l. beneath the Vitismor field. Temperature logs of wells in the Vitismor field reveal that the current reservoir temperature at depths 0.1 to 0.7 km b.s.l. is isothermal and about 200 °C (Fig. 12). Analysis of drill cuttings performed by Mortensen *et al.* (2014) indicates that the top of R1 coincides with the transition into the chlorite–epidote alteration zone where the formation temperature once exceeded 220 °C. Although high temperature fluids may be attributed to high resistivity (e.g. Ucok *et al.* 1980; Ussher *et al.* 2000) this cannot be the case here because the upper reservoir temperature of Vitismor is only about 200 °C. This observation is consistent with the pattern that resistivity in geothermal fields in Iceland is mainly controlled by alteration mineralogy, as opposed to permeability. In addition to R1, high resistivity in Sudurhlidar corresponds to resistive epidote–actinolite alteration, and high resistivity in Leirbotnar corresponds to chlorite–epidote alteration.

Low resistivity chimney (C2)

This moderately conductive feature appears to connect the deeper conductor (C3) to the surface. A similar feature was observed in the 1-D resistivity models of Árnason *et al.* (2008) and the 3-D models of Gasperikova *et al.* (2015) and Rosenkjaer *et al.* (2015). There are two vertical low resistivity anomalies that flank the path of IDDP-1 and merge with the conductor C3 at a depth of approximately 1.5 km b.s.l. The location of C2 agrees well with the Hveragil fault system,

Downloaded from https://academic.oup.com/gji/article/220/1/541/5587733 by guest on 30 March 2022

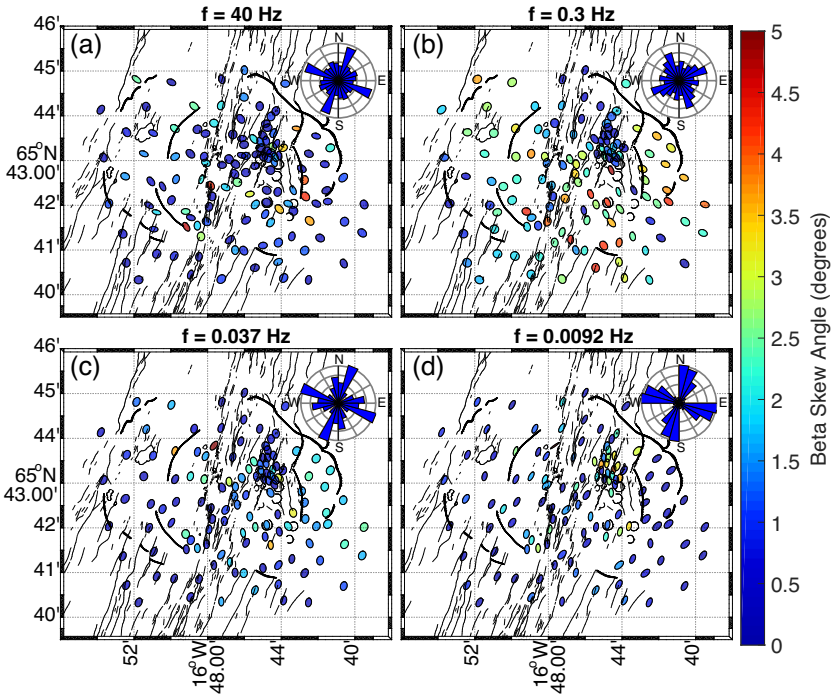

Figure 7. Map view of Krafla MT phase tensor ellipses at four frequencies. Inset polar histograms show the major and minor axis directions of phase tensor ellipses for all stations. The grey circles in the histograms are increments of 10 stations, with the largest circle for 40 stations. The major axis direction indicates the strike direction, i.e. the preferred direction of electric current flow. At 40 Hz there is some variation in strike direction from station to station because the data are only sensitive to shallow depths, yet there is a pronounced N20° E strike direction that agrees well with the mapped fissures. At a frequency of 0.3 Hz there is no clear predominant strike direction. Many stations have a skew angle greater than 3° which is indicative of 3-D resistivity structure at this frequency. At frequencies of 0.037 and 0.0092 Hz the alignment of the ellipses with the NNE–SSW direction of the fissure swarm and low skew angles suggest that the data are relatively 2-D at lower frequencies.

which divides the Vitismor and Leirbotnar fields from the Sudurhlidar field. As previously mentioned, increased porosity within the Hveragil fault system can host aqueous fluids that could significantly decrease resistivity. Weisenberger *et al.* (2015) also reported a major feed zone in Sudurhlidar associated with a felsic intrusion complex from 0.2 to 0.6 km b.s.l., coinciding with the elevation of C2. C1 and C2 appear connected due to the fact that MT has a limited ability to resolve the lower boundary of conductors. However, the chlorite–epidote zone beneath Sudurhlidar is observed at 0.3 to 0.2 km a.s.l. which effectively constrains the lower elevation of the clay layer C1 (Weisenberger *et al.* 2015). Thus, the low resistivity of C2 is not due to the clay layer and can instead be attributed to aqueous fluids within the permeable Hveragil fault system.

Pope *et al.* (2016) analysed isotope ratios of geothermal fluids from Krafla. Their hydrogeological model of Krafla describes the same meteoric source for Leirbotnar and Sudurhlidar, but with different degrees of phase separation and mixing with magmatic gases. In our resistivity model, a low to intermediate resistivity zone (C2) between Leirbotnar and Sudurhlidar matches the location of the Hveragil fault system, which agrees with their interpretation of Hveragil as an upflow zone separating these two subfields. Hveragil appears as a low resistivity feature because it is a subvertical pathway for hot geothermal fluid and magmatic gas ascending from the two-phase reservoirs below Sudurhlidar, Vitismor, and Leirbotnar.

Upper crustal conductor (C3)

Feature C3 is an extensive low resistivity zone beneath the northern part of the inner caldera. Its lateral dimensions are approximately 5 km by 5 km; however, the northern edge is not well-constrained because it extends outside of the MT survey area. C3 domes upward to a depth of about 1.6 km b.s.l., and appears to extend to greater than 5 km b.s.l., although the lower limit is not well-constrained by the MT data. In Figs 9 and 10 the bottom of IDDP-1 intersects a low resistivity zone that connects features C2 and C3. We believe the feature C3 has two possible interpretations:

(1) A zone of partial melt
(2) A zone of dehydrated chlorite and/or epidote alteration minerals that have formed magnetite (Manthilake *et al.* 2016; Hu *et al.* 2017; Nono *et al.* 2018).

Because many factors can contribute to a low resistivity, it is unclear if C3 is due to just one, or a combination of the two interpretations stated above. If C2 is an up-flow zone of two-phase geothermal fluid (>340 °C) related to the permeable Hveragil fault system, then it makes sense that it would be connected to a deeper magmatic heat source. However, it is unlikely that the top of C3 corresponds to the top of a large, homogeneous magma body. Einarsson (1978) inferred a 3 km depth to the top of the magma body from shear wave attenuation, which is about 1 km deeper than the bottom of IDDP-1. C3 is also mostly to the north of the *S*-wave shadows from Einarrson (1978) at 1.6 to 2.1 km b.s.l. (see Fig. 10). Although the spatial correlation is not exact, it must be noted that the seismic study had limited resolution and different station coverage to the MT survey. Einarsson (1978) stated that the southern boundaries of the *S*-wave shadows are better constrained than the northern ones. Only one of the three seismic stations in the study (station SN) was located to the north of the caldera and would receive many ray

Downloaded from https://academic.oup.com/gji/article/220/1/541/5587733 by guest on 30 March 2022

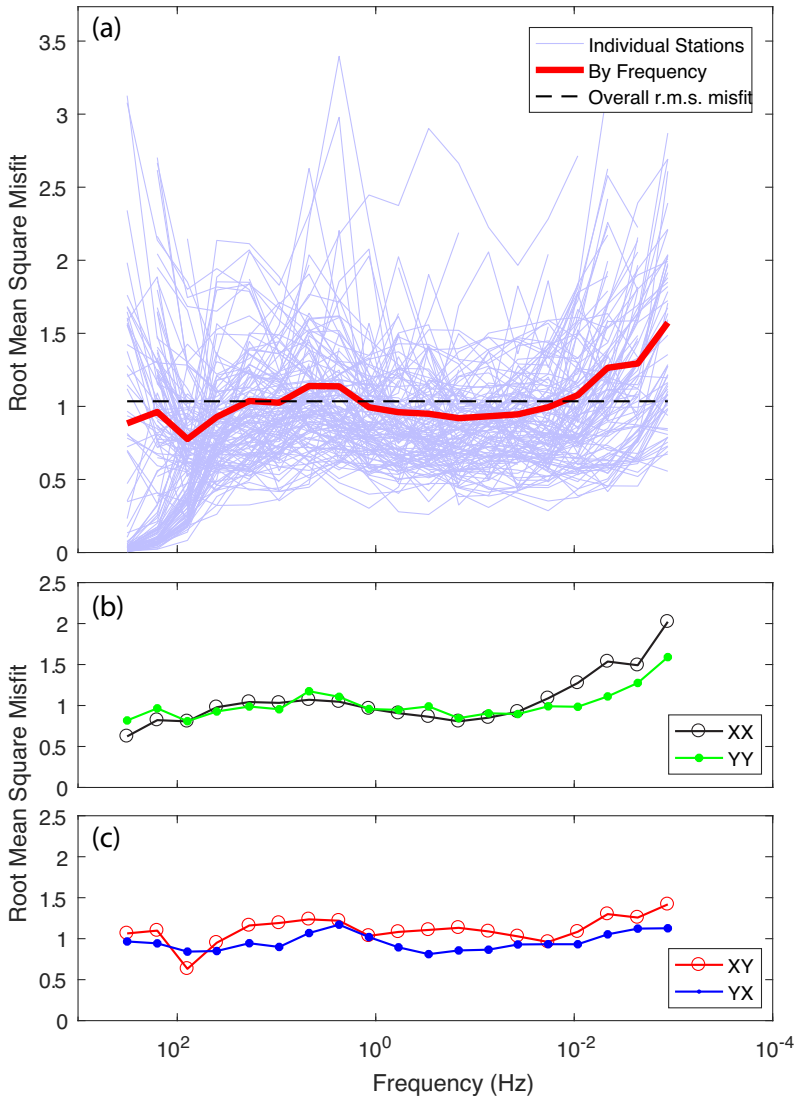

Figure 8. Root mean square (r.m.s.) misfit of the measured and calculated MT data from the unconstrained 3-D inversion. (a) r.m.s. misfit by frequency for each individual station; the overall misfit for each frequency and the overall inversion misfit are shown in red and dashed black lines, respectively. (b) diagonal and (c) off-diagonal impedance components r.m.s. misfit by frequency.

paths passing under the north caldera. Most of the arrivals were critically refracted and may not have sampled a deep attenuating magma body. Seismic tomography by Schuler *et al.* (2015) revealed a low v_p/v_s ratio anomaly at the bottom of IDDP-1 that they interpreted as a zone of superheated steam above the rhyolitic magma body. This effectively rules out an expansive zone of partial melt at 1.6 km b.s.l., which would require an elevated v_p/v_s ratio. However, we cannot eliminate the possibility that IDDP-1 intersected a small magma body (dyke or sill), which would not provide as strong of a geophysical anomaly as a larger magma body. We will assess the MT data response to synthetic smaller magma bodies in the next section.

Recent work has shown that dehydration of chlorite and epidote alteration minerals (Manthilake *et al.* 2016; Hu *et al.* 2017; Nono *et al.* 2018) leads to decreased rock resistivity at high temperatures and pressures. Nono *et al.* (2018) performed resistivity measurements on Icelandic rocks at high temperature (200 to 700 °C) and pressure (70 MPa) and showed that destabilization of the chlorite and epidote alteration minerals above 500–600 °C resulted in an irreversible resistivity decrease from about 1000–100 000 Ωm to about 3–30 Ωm. The resistivity of C3 falls within this resistivity range. Mortensen *et al.* (2014) estimated that the formation temperature at the bottom of IDDP-1 is about 500 °C, which agrees with the onset temperature of chlorite/epidote destabilization reported by Nono *et al.* (2018). This suggests that destabilization of the alteration minerals may occur below the bottom of IDDP-1. Note that the pressure at the bottom of IDDP-1 is between hydrostatic and lithostatic pressures (21 to 51 MPa; Elders *et al.* 2011) which is lower than the experimental 70 MPa pressure of Nono *et al.* (2018). However, at these conditions temperature has a much larger impact on electrical resistivity than pressure (e.g. Manthilake *et al.* 2016; Hu *et al.* 2017).

Upper crustal conductors have been observed beneath other geothermal fields in Iceland. Large low resistivity (<10 Ωm) zones have been detected 4 km b.s.l. at Hengill (Árnason *et al.* 2010) and about 3 km b.s.l. at Námafjall (Karlsdóttir *et al.* 2015). Seismic tomography at Hengill did not reveal a velocity anomaly consistent with the presence of partial melt (Tryggvason *et al.* 2002).

Downloaded from https://academic.oup.com/gji/article/220/1/541/5587733 by guest on 30 March 2022

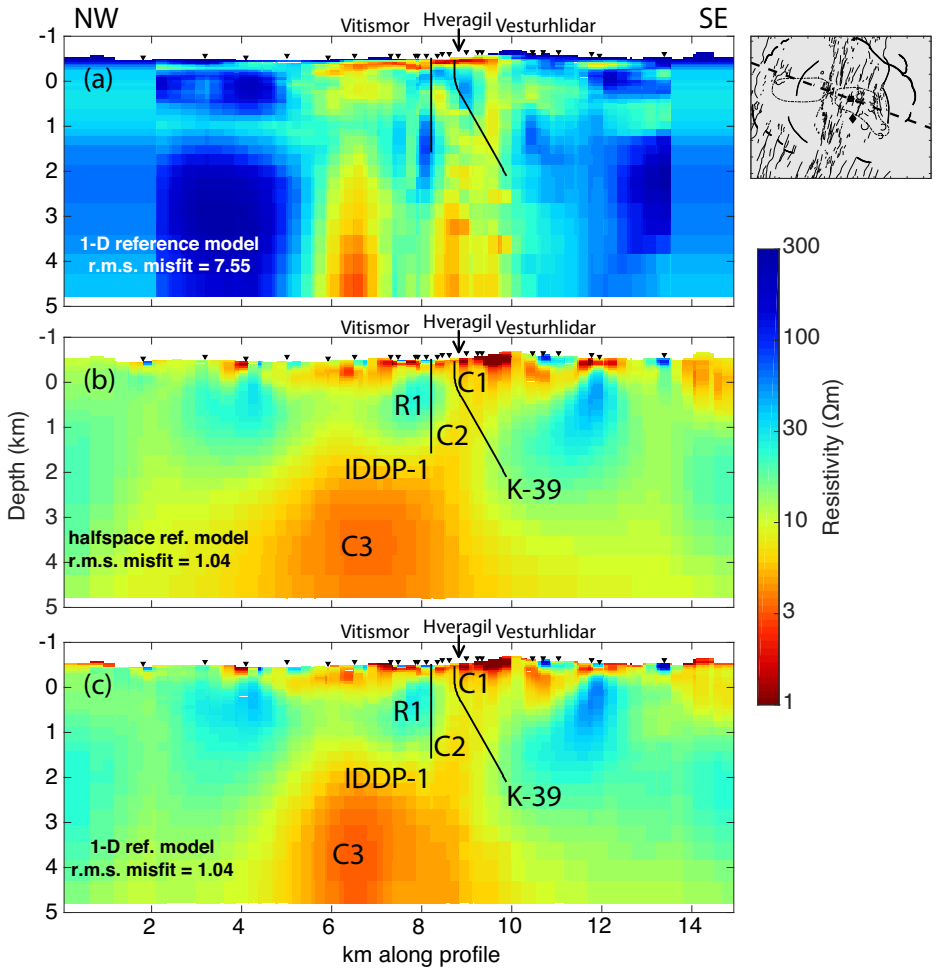

Figure 9. (a) Northwest to southeast slice through the interpolated 1-D prior model of Árnason et al. (2008); (b) same model slice through the 3-D MT inversion with a 10 Ωm half-space as the prior model; (c) same slice through the 3-D MT inversion using the interpolated 1-D MT models as a prior model. See inset map and Fig. 1 for the location of profile trace A–A'. Note that the 1-D model in (a) has been interpolated onto the 3-D mesh used in our inversions. The path of the two wells that intersected rhyolite magma, IDDP-1 and K-39, are shown in black. The path of K-39 is projected onto the profile from about 1 km to the south.

Destabilization of chlorite and epidote may explain the conductors below these geothermal fields.

Other studies at Krafla have proposed more complicated geometries for the magmatic system. Schuler *et al.* (2015) imaged a low v_p/v_s ratio anomaly at the depths that IDDP-1 and K-39 intersected rhyolitic magma. They suggested that the anomaly was due to a region of superheated steam overlying a region of melt. Although our resistivity model contains a moderately low resistivity zone at the bottom of IDDP-1, a zone of superheated steam would not be expected to produce a low resistivity anomaly (e.g. Ussher *et al.* 2000). Their vertical grid spacing of 0.5 km is about twice as large as the cell size used in our inversions, so it is possible that the low v_p/v_s ratio anomaly is not coincident with the top of C3 in our resistivity model. Axelsson *et al.* (2014) modelled the possibility that a small magma intrusion was emplaced during the Krafla Fires of 1975 to 1984 that was later intersected by IDDP-1. Though they were unable to confirm or disprove the idea, deformation-induced melt segregation could be a mechanism of transporting relatively viscous, immobile rhyolitic melt (Jónasson 2007).

The origin of rhyolite melt beneath Krafla was confirmed by studies of recovered silicic glass. Hydrogen and oxygen isotope analysis of the IDDP-1 rhyolite showed that the rhyolite was formed by re-melt of hydrothermally altered basalt (Elders *et al.* 2011; Zierenberg *et al.* 2013). Well K-39, about 2 km to the southeast of IDDP-1, intersected a thin sill (~20 m) of rhyolite melt at approximately 2.1 km b.s.l. Major element analysis of the quenched silicic glass recovered by well K-39 suggested that the melt also formed by partial melting of hydrothermally altered basalt (Mortensen *et al.* 2010). Because the rhyolite forms from re-melting of basalt, Jónasson (2007) suggested that the rhyolite magma forms an intrusive complex beneath a central volcano, rather than a single, large magma chamber. Thus, IDDP-1 and K-39 may have intersected an intrusive complex with a number of small, rhyolite magma bodies that overlie the basaltic magma body inferred at about 3 km depth (Figs 9 and 10).

These models with multiple, small magma bodies are inconsistent with the feature C3 in the resistivity model shown in Figs 9 and 10. A key issue to understand is the resolution of the MT method. Because this method uses signals that diffuse in the Earth, it can be difficult to distinguish relatively small bodies at depth. The fact that the rhyolite sill intersected by well K-39 was about 20 m thick suggests that rhyolite magma bodies beneath Krafla are too small to be resolved at such depth by the MT method. In addition, well K-25 is located 200 m southwest of IDDP-1 but did not encounter

Downloaded from https://academic.oup.com/gji/article/220/1/541/5587733 by guest on 30 March 2022

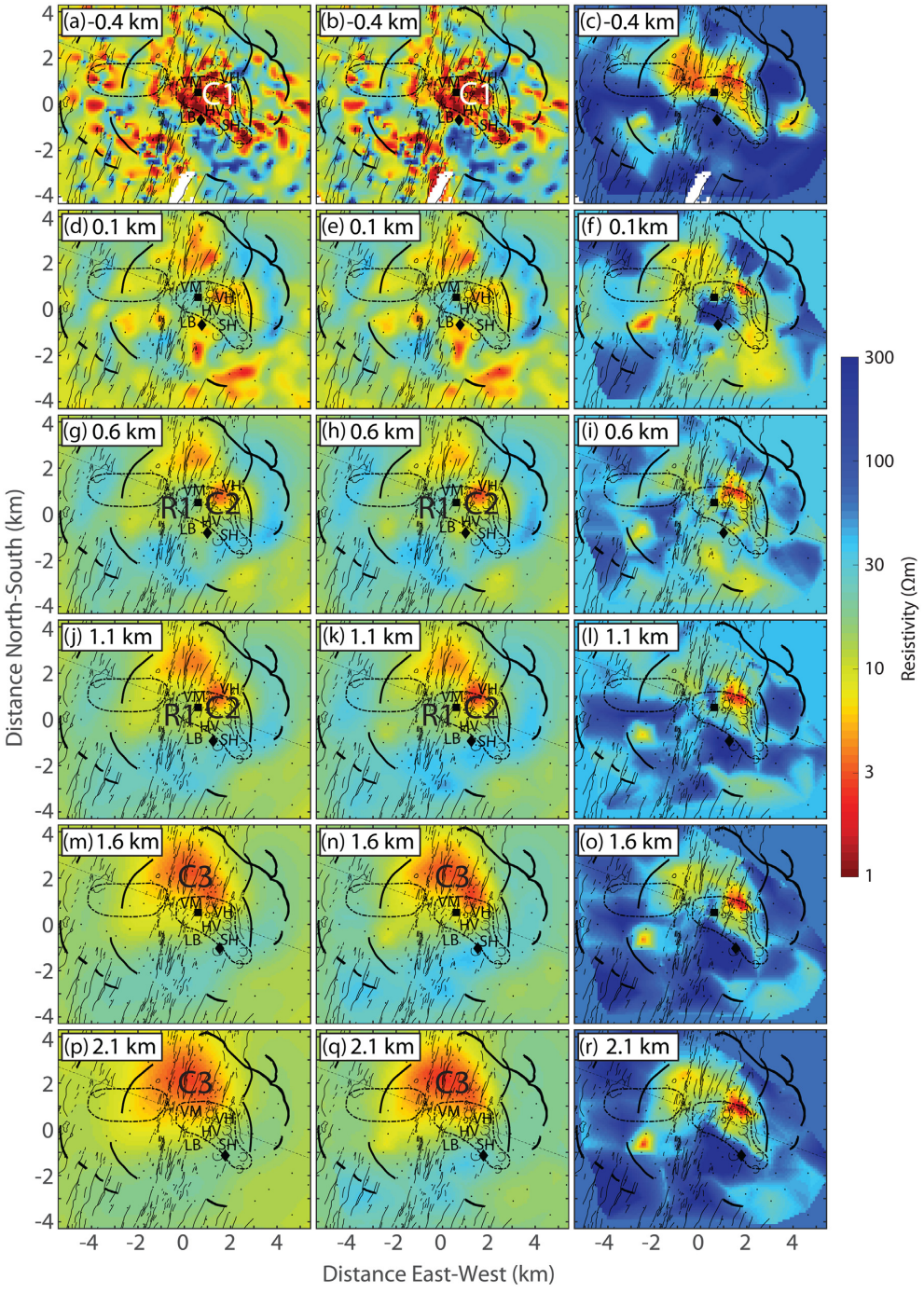

Figure 10. Horizontal slices through resistivity models at elevations of –0.4 km, 0.1 km, 0.6 km, 1.1 km, 1.6 km and 2.1 km below sea level. Left-hand column (a,d,g,j,m,p): unconstrained inversion resistivity model with a 10 Ωm half-space prior model; centre column (b,e,h,k,n,q): constrained inversion resistivity model with the 1-D prior model; right-hand column (c,f,i,l,o,r): the interpolated 1-D resistivity model of Árnason et al. (2008). The slices at 1.6 and 2.1 km elevation correspond to the depths that the IDDP-1 and K-39 wells intersected rhyolitic magma, respectively. The thick black lines are the inner and outer calderas, thin lines are faults and fissures; dashed shapes are the shear wave shadows from Einarsson (1978), the black square is IDDP-1, the black diamond is well K-39. VM = Vitismor; LB = Leirbotnar; HV = Hveragil; SH = Sudurhlidar; VH = Vesturhlidar. See the main text for interpretation of the resistivity features R1, C1, C2 and C3.

rhyolite magma at its total depth of 1.55 km b.s.l. The inability of MT to detect such small-scale bodies may explain why the bottom of K-39 does not coincide with a low resistivity feature in the model (Figs 9 and 10). The next section will address this issue with a set of resolution tests to quantify the size and resistivity of possible magma bodies at Krafla.

5.2 Comparison of the unconstrained and constrained 3-D MT inversions

Fig. 9(b) shows the vertical slice A–A' through the 3-D resistivity model from the unconstrained inversion (same uniform starting and prior models). Fig. 9(c) shows the same slice through the 3-D resistivity model from the constrained inversion (uniform starting model

Downloaded from https://academic.oup.com/gji/article/220/1/541/5587733 by guest on 30 March 2022

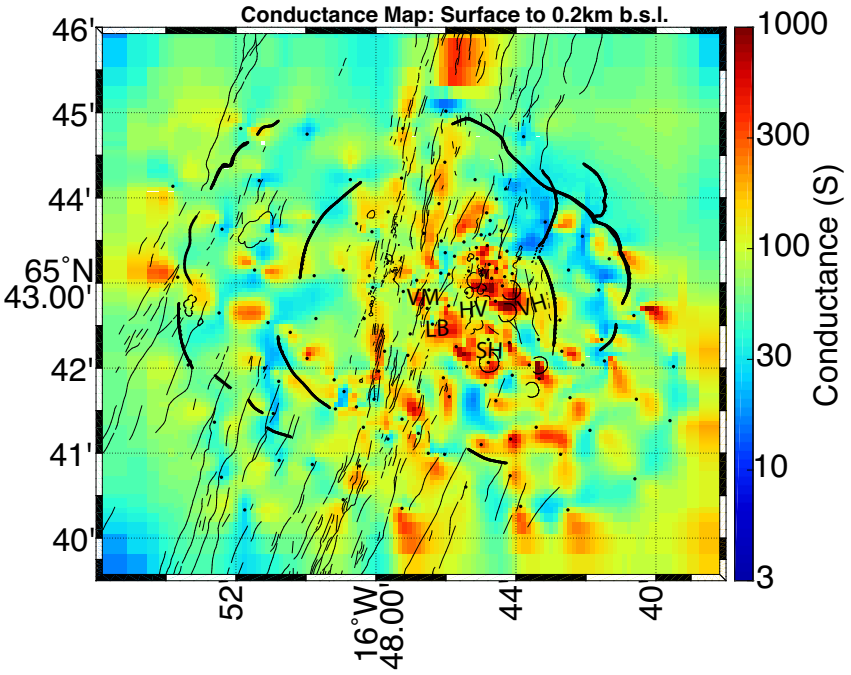

Figure 11. Integrated conductivity (conductance) in the unconstrained resistivity model from the surface to 0.2 km b.s.l. A high conductance (>300 S) in the inner caldera coincides with the shallow clay layer. VM = Vitismor; LB = Leirbotnar; HV = Hveragil; SH = Sudurhlidar; VH = Vesturhlidar.

with 1-D prior model). It is clear that with no *a priori* information, the resulting resistivity model is quite similar to the one obtained with the interpolated 1-D model as a prior model. Compared to the inversion with the interpolated 1-D prior model (Fig. 9), the inversion with no *a priori* information is smoother at depths below 1 km (depths are below sea level). In the constrained model (Fig. 9c), the conductor C3 below 1 km depth has a more limited lateral extent, as seen in the 1-D prior model (Fig. 9a). Horizontal slices through the two inversion models also show very similar resistivity structures (Fig. 10). The constrained inversion model appears to keep high resistivity structures such as R1 from the 1-D prior model at elevations of 1.1 and 1.6 km b.s.l. (Fig. 10), which is expected of the high-temperature geothermal reservoirs at those depths. The slices at 1.6 and 2.1 km b.s.l. coincide with the depths that the IDDP-1 and K-39 wells intersected rhyolitic magma, respectively.

5.3 Comparison with previous MT inversions

The resistivity models of the Krafla volcanic field presented in this paper share a number of features with the 3-D models published by Gasperikova *et al.* (2015) and Rosenkjaer *et al.* (2015). These include:

(1) Resistive, unaltered basalt and low resistivity clay layers (C1) near the surface

(2) A resistive chlorite–epidote core (R1) at depths of −0.5 to 2 km b.s.l.

(3) Subvertical, low resistivity feature (C2) flanking IDDP-1 to the northwest and east

(4) A low-resistivity feature (C3) at 3 km b.s.l. below the northern part of the inner caldera

Although our resistivity model contains the same major features as the previous authors' model, there are some notable differences. In the models of Gasperikova *et al.* (2015) and Rosenkjaer *et al.* (2015), IDDP-1 is flanked by low-resistivity structures to the west and northwest, and the bottom of IDDP-1 is located in a resistive feature interpreted as the chlorite–epidote core. Their interpretation was that IDDP-1 intersected a small magma body that was too small to be resolved with MT. However, in our model the bottom of IDDP-1 intersects a low resistivity region where the features C2 and C3 meet. We have interpreted this region as a zone of high permeability where primary aquifer fluids mix with magmatic fluids and gas from the deeper magma body (C3). There are a few differences in our inversion strategies that might help explain the disparity in our models. Rosenkjaer *et al.* (2015) summarized the inversion parameters used to obtain the resistivity models in their paper and in Gasperikova *et al.* (2015). A significant difference from our model is the minimum cell size; in their inversions the smallest cell size varied from 250 m × 250 m × 50 m to 300 m × 300 m × 8 m compared to our 100 m × 100 m × 30 m cells. This results in our model containing over twice as many cells in the horizontal directions (north–south and east–west). Due to the nonlinearity of the inversion process, and the fact that different inversion algorithms were used, it is difficult to determine if the difference in cell size would lead to differences in our models at about 2 km depth. However, we believe that the 100 m horizontal cells are required to model near-surface resistivity variations between MT stations that are only about 300 m apart. Because we are not explicitly solving for galvanic distortion, the small cells between MT stations allow the inversion to fit distorted MT data by placing small features near the surface. The low r.m.s. misfit at high frequencies suggests that the model surface is sufficiently discretized to fit the distortion in the MT data (Fig. 8).

The resistivity models presented in Gasperikova *et al.* (2015) and Rosenkjaer *et al.* (2015) were derived from inversion of the off-diagonal impedance elements, while our inversions used the full impedance tensor. The diagonal impedance elements in many

Downloaded from https://academic.oup.com/gji/article/220/1/541/5587733 by guest on 30 March 2022

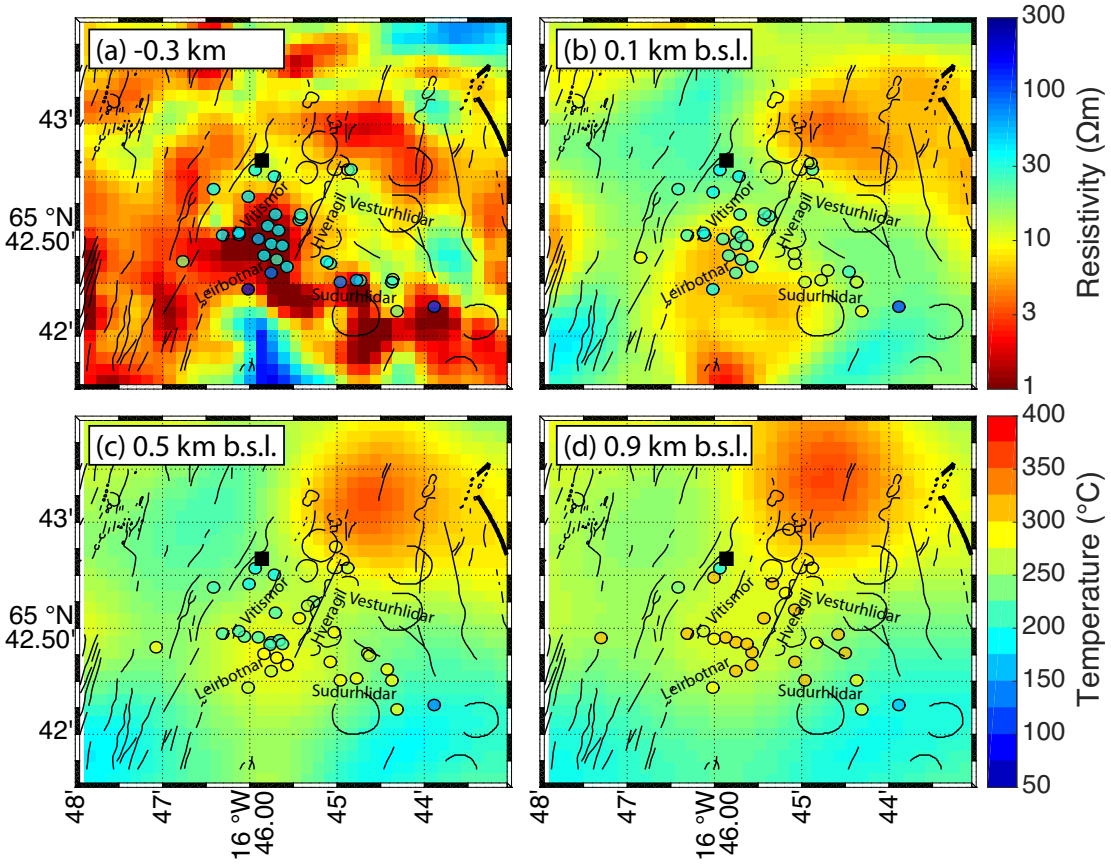

Figure 12. Map view of well temperature and model resistivity in the Krafla geothermal field at four depths: (a) −0.3 km, (b) 0.1 km, (c) 0.5 km and (d) 0.9 km b.s.l. Note the resistivity colour bar corresponds to the model resistivity (background shading) and the temperature colour bar corresponds to the well temperatures (coloured circles). Each coloured circle is the location of a well track at the specified depth. In (a) temperatures below 200 °C correspond to the shallow, two-phase reservoirs. The well temperatures below 200 °C correlate with the low resistivity clay layer. At intermediate depths in (b) and (c) temperatures in the Leirbotnar and Sudurhlidar fields are >225 °C reflecting the superheated reservoir, but only about 200 °C in the Vitismor field. This corresponds to the nearly isothermal reservoir beneath Vitismor. Below 0.9 km in (d) most well temperatures are above 300 °C, corresponding to superheated reservoirs. Higher resistivity is due to chlorite and epidote alteration minerals formed above 220 °C. The black square indicates the location of IDDP-1 (no temperature log available). The black lines are faults, fissures and craters.

MT data sets are at least an order of magnitude smaller than the off-diagonal elements; thus their importance in 3-D inversion is still under debate (Miensopust 2017). For example, Newman *et al.* (2008) justified omitting the diagonal elements because of their low magnitude, and thus low signal-to-noise ratio. Lindsey & Newman (2015) inverted the Krafla MT data to demonstrate their sequenced inversion workflow. They justified neglecting the diagonal impedance elements because only 15 per cent of the data had a diagonal to off-diagonal ratio greater than 0.1. Because 80 per cent of these data were below 0.1 Hz, they claimed that the off-diagonal elements were sufficient for imaging the upper ∼3 km below Krafla. However, we believe that the diagonal elements should be inverted because the data below 0.1 Hz are sensitive to the deep conductors in the vicinity of IDDP-1. This can be seen in the map view of MT data in Figs 2–5 and the data curves in Fig. 6 that show a decrease in apparent resistivity at frequencies below 0.1 Hz. We have inverted the Krafla MT data using only off-diagonal elements and found that the main interpreted features (R1, C1, C2 and C3) are still present in the resistivity model. Although a qualitative interpretation of the resistivity model might remain unchanged, we note that the full impedance tensor data calculated from the off-diagonal derived resistivity model (1) poorly fit the observed diagonal impedance components; and (2) did not reproduce the high (>3°) beta skew angles at intermediate frequencies. Other authors have presented benefits of inverting the full tensor (e.g. Patro & Egbert 2011; Kiyan *et al.* 2013).

Besides the differences in model discretization and choice of impedance tensor elements, our choice of data frequencies, number of frequencies, number of stations and uniform initial starting model vary slightly from those of Gasperikova *et al.* (2015) and Rosenkjaer *et al.* (2015). However, these choices are dependent on the individual user and available software, and a more rigorous study is required to determine their exact effects on the inversion resistivity model.

6 MT DATA SENSITIVITY TO THE IDDP-1 RHYOLITE MAGMA

In this section we will assess why MT did not detect the presence of rhyolite melt prior to drilling IDDP-1. Our resolution tests will address two possibilities: (1) the location of the rhyolitic magma directly beneath the clay layer makes it difficult to be resolved with the MT method; and (2) the rhyolite magma body has a relatively high resistivity and/or is relatively small and does not appear as an anomaly in the resistivity model. First we use petrological information about the IDDP-1 rhyolite and relations from laboratory melt studies to constrain a range of possible resistivity values, assuming

Downloaded from https://academic.oup.com/gji/article/220/1/541/5587733 by guest on 30 March 2022

a homogeneous magma body. Next we add anomalies into our 3-D inversion model to simulate rhyolite magma bodies with a range of simple geometries. We tested anomalies with three different geometries and six resistivity values, for a total of 18 resolution tests. In each test, we calculated the predicted MT data for the edited model and compared this with the response of the MT inversion model. We use two approaches to quantify the difference between the two sets of data: (1) the change in r.m.s. misfit, and (2) an asymptotic *p*-value from the two-sample Kolmogorov–Smirnov (K–S) statistical test. To our knowledge, this is the first published use of the K–S test to judge a change in MT data fit between two resistivity models.

6.1 IDDP-1 magma body resistivity

An important part of this modelling study is to estimate the expected resistivity of the rhyolite melt. This is required to determine whether the contrast between the magma body and the host rock is sufficient for an MT survey to detect the magma body as a zone of low resistivity. Gibert *et al.* (2017; published in: Levy 2019) measured the electrical resistivity of melted rhyolite from the Hrafntinnuhryggur, an obsidian ridge produced by subglacial fissure eruption, southeast of the southern slopes of Mt. Krafla (labelled in Fig. 1 as Rhyolite 115 to 11.7 ka). The rhyolite resistivity was measured to be 0.8 to 1.2 Ωm at temperatures of 900 to 1000 °C. We further investigate the Krafla rhyolite resistivity using data from additional lab experiments.

We can estimate the resistivity of the IDDP-1 magma body in order to understand whether or not it could be detected by the MT data. As seen in Figs 9 and 10, the region at the bottom of IDDP-1 has a resistivity of about 7 Ωm, which is relatively resistive. Following the relation of Guo *et al.* (2016), a pure rhyolite melt can be relatively resistive (>1 Ωm) under particular conditions such as low water content, low melt fraction or limited connectivity.

We estimated the resistivity range of the rhyolitic magma encountered by IDDP-1 using the experimental melt relations of Guo *et al.* (2016) and petrological analyses by Elders *et al.* (2011) and Zierenberg *et al.* (2013) in order to provide an input for the resolution tests. Fig. 13 shows values of electrical resistivity of pure rhyolite melt for varying temperature and per cent wt H_2O. The figure demonstrates that increasing temperature and/or per cent wt H_2O decreases the melt resistivity. Additionally, it is possible that a rhyolite melt with a high per cent wt H_2O at a low temperature could have the same resistivity as a melt with lower per cent wt H_2O at a higher temperature. Note that the pressure at the bottom of IDDP-1 is between hydrostatic and lithostatic (Elders *et al.* 2011) and its influence on electrical resistivity is negligible in the range ∼20 to 50 MPa. The dashed rectangle denotes the possible range of resistivity for the rhyolite melt based on temperature and per cent wt H_2O estimates by Elders *et al.* (2011) and Zierenberg *et al.* (2013). This gives a minimum of 0.6 Ωm (black circle) and a maximum of 0.9 Ωm (black square) for the melt resistivity. Our calculated pure rhyolite melt resistivity values agree with the 0.8 to 1.2 Ωm measured by Gibert *et al.* (2017). If possible, a direct resistivity measurement of the rhyolite recovered from IDDP-1 would eliminate the need to use empirical relations to estimate the resistivity.

Once the melt resistivity has been calculated, it is necessary to estimate the bulk resistivity of the rock, which is a mixture of melt and crystals. The bulk resistivity can be estimated using the empirical Modified Archie's Law (Glover *et al.* 2000) to relate melt and bulk resistivity to melt fraction. The bulk conductivity σ_b is related to the rock matrix conductivity σ_r and melt (fluid) conductivity σ_f by:

$$\sigma_b = \sigma_r (1-\phi)^p + \sigma_f \phi^m, \tag{5}$$

where m is the cementation factor, ϕ is the melt fraction and

$$p = \frac{log(1-\phi^m)}{log(1-\phi)}. \tag{6}$$

The cementation factor m defines the connectivity of the melt and is a function of pore geometry, distribution and dihedral (wetting) angle (e.g. Yoshino *et al.* 2010). Commonly m is in the range of 1 (well connected) to 2 (poorly connected). Some studies suggest that silicate melt is relatively well-connected at intermediate melt fractions. Rosenberg & Handy (2005) found that melted granite was well-connected at melt fractions greater than 0.07. Ten Grotenhuis *et al.* (2005) observed that basaltic melt occupied grain boundary layers as opposed to only triple junctions as melt fraction increased from 0.01 to 0.1. We use $m = 1.5$ assuming a moderate degree of interconnected melt. However, we found that choosing a value of m in the range 1 to 2 does not affect the resistivity enough to change our interpretation. Fig. 14 shows contours of bulk resistivity computed from Modified Archie's Law for a range of melt resistivity and melt fraction. We used a rock matrix conductivity (σ_r) of 0.001 S m^{-1} for these calculations, though we observe negligible differences in bulk resistivity when the rock matrix is at least three orders of magnitude more resistive than the melt (i.e. $\sigma_r << \sigma_f$). A low melt fraction might be expected for Krafla rhyolite due to inferred high viscosity and a near-solidus state (Jónasson 2007). However, the recovered IDDP-1 rhyolite was a nearly aphyric glass (Elders *et al.* 2011; Zierenberg *et al.* 2013) which indicates a high melt fraction. In our analysis we make no assumption about melt fraction and consider the range from 0.1 to 0.9. The range of rhyolite melt resistivity constrained from Guo *et al.* (2016) is 0.6 to 0.9 Ωm. These minimum and maximum estimates of melt fraction and melt resistivity are shown in Fig. 14 as dashed lines. Using these bounds on melt resistivity, and considering a melt fraction range of 0.1 to 0.9, the rhyolite encountered by IDDP-1 has a maximum bulk resistivity of about 30 Ωm and a minimum of about 0.7 Ωm. In the next section we will test if the MT data are sensitive to magma bodies in this resistivity range.

This resistivity range is higher than resistivity estimates of silicic magma reservoirs such as those of the New Zealand Taupo Volcanic Zone (Heise *et al.* 2010) and the Laguna del Maule volcanic field in Chile (Cordell *et al.* 2018). Heise *et al.* (2010) estimated a resistivity of ∼ 0.3 Ωm and a melt fraction of ∼50 per cent for a silicic plume beneath the Taupo Volcanic Zone, and Cordell *et al.* (2018) estimated a resistivity of ∼1 Ωm and a melt fraction of <35 per cent for a long-lived silicic magma chamber below Laguna del Maule. In particular, the relatively low 1.77 per cent wt H_2O of the IDDP-1 rhyolite contributes significantly to its higher resistivity (Elders *et al.* 2011). Note that due to the difference in size, temperature, depth and water content, it is impossible to directly compare these melt fraction estimates to that of the IDDP-1 rhyolite. Because these silicic magma chambers are long-lived features they may be close to a crystal mush state with a low to intermediate melt fraction. However, Elders *et al.* (2011) and Zierenberg *et al.* (2013) noted that the recovered IDDP-1 rhyolite was aphyric, which indicates a high melt fraction. This comparison demonstrates how a wet magma with low melt fraction can have a similar resistivity as a dry magma with high melt fraction (i.e. Fig. 14).

Downloaded from https://academic.oup.com/gji/article/220/1/541/5587733 by guest on 30 March 2022

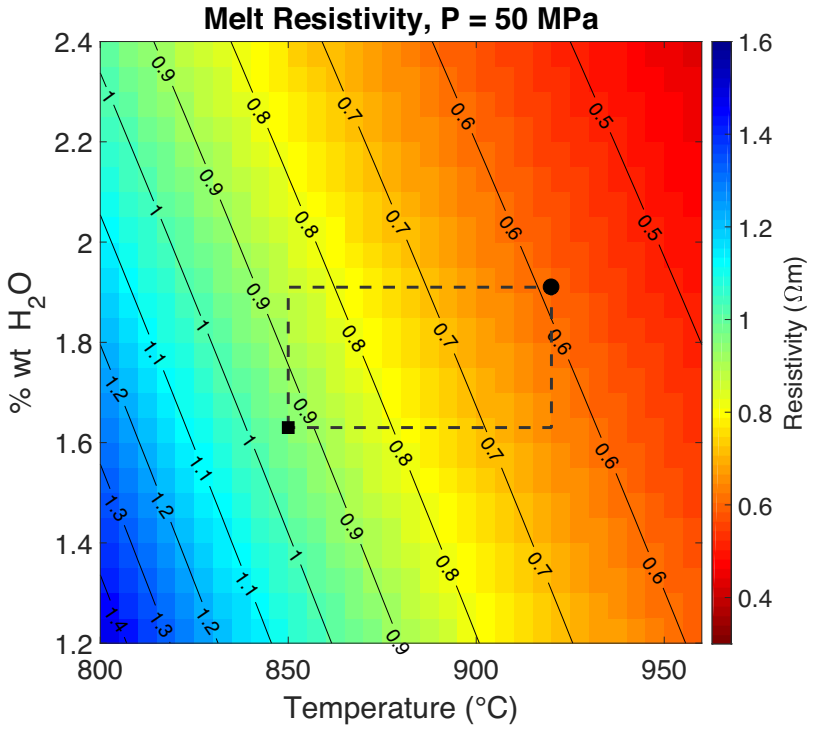

Figure 13. Contour lines of electrical resistivity as a function of temperature (°C) and per cent wt H_2O calculated from the relation of Guo et al. (2016). The dashed line shows ranges of temperature from Zierenberg et al. (2013) and per cent wt H_2O from Elders et al. (2011). The black square is the maximum resistivity from these bounds; the black circle is the minimum resistivity.

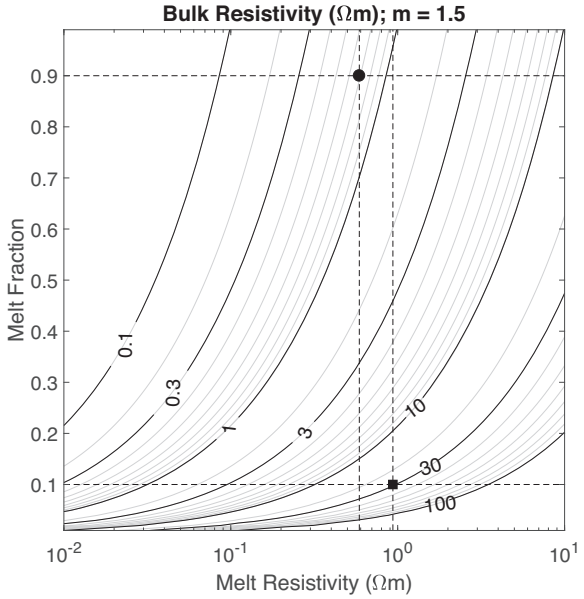

Figure 14. Logarithmic contours of Krafla rhyolite bulk resistivity as a function of melt fraction and melt resistivity computed from Modified Archie's Law (Glover et al. 2000). Vertical dashed lines: minimum and maximum resistivity of the Krafla rhyolite computed from relation of Guo et al. (2016); horizontal dashed lines: range of melt fraction (0.1 to 0.9) considered in our synthetic tests. The black square and black circle denote maximum and minimum estimated bulk resistivity of Krafla rhyolite, respectively.

6.2 Resolution tests

These tests are needed because it is possible that the conductor caused by the magma body is not being correctly imaged. This can occur for a number of reasons:

(1) the presence of C1, a high conductance (>300 S) layer that screens the EM signals, and

(2) the magma body is relatively resistive and/or has a small resistivity contrast from the surrounding rock. The diffusive physics of MT means that a small, low resistivity anomaly can go undetected. The approach used in the inversion assumes diffusive signal propagation and generates a smooth resistivity model with minimum structure.

To implement the resolution tests, the unconstrained resistivity models in Figs 9 and 10 were edited to include different geometries of a low resistivity zone which represents a crustal magma body. These low resistivity zones (i.e. magma bodies) were added at a depth of 1.6 km b.s.l. based on the depth at which the IDDP-1 well intersected magma. This corresponds to the upper edge of the conductive feature C3. Fig. 15 shows the outlines of the three magma bodies considered in these tests. The three magma bodies were designed to represent a thin sill (B1), a small cubic magma body (B2) and a larger cubic magma body (B3). In the previous section we determined that the magma body encountered by IDDP-1 has a resistivity between 0.7 to 30 Ωm with a melt fraction of 0.1 to 0.9. To investigate this resistivity range each of the three magma body geometries was assigned six different bulk resistivity values between 0.1 and 30 Ωm. The 18 combinations of geometry and resistivity that were tested are listed in Table 1. Table 1 also lists the conductance for each test magma body. The conductance

Downloaded from https://academic.oup.com/gji/article/220/1/541/5587733 by guest on 30 March 2022

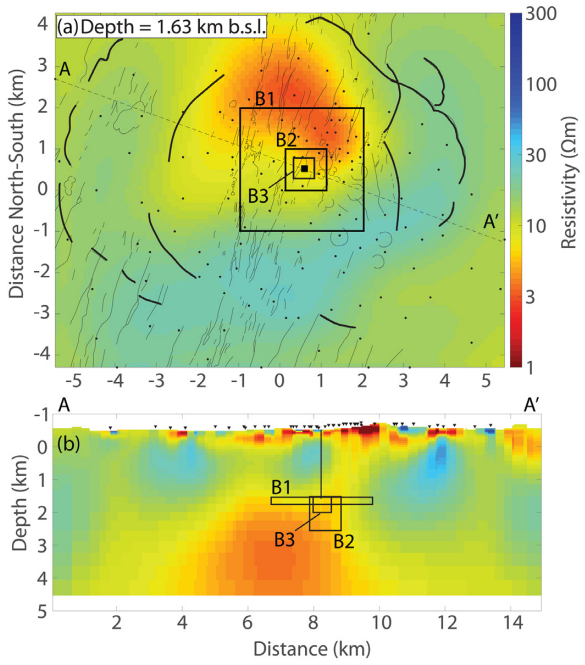

Figure 15. Outlines of test magma bodies in (a) map view and (b) vertical slice through A–A'. See Table 1 for magma body dimensions and resistivities.

of an arbitrarily shaped body can be calculated with the relation

$$C = \frac{\sigma A}{L}, \tag{7}$$

where A is the cross-sectional area and L is the body length (e.g. Yoshino 2018). In a 1-D layered Earth, where conductivity only varies in the z-direction, eq. (7) simplifies to the conductivity multiplied by the thickness of the feature (e.g. Bai *et al.* 2010; Yang *et al.* 2015). However, in the 3-D case the spatial dimensions of the body may be different in three directions. We can calculate the conductance of the B1, B2 and B3 test anomalies by considering electrical current flow in the north–south direction, and using the dimensions from Table 1. Using eq. (7), the conductances of the thin sill, small magma cube and large magma cube range from 8.3 to 2500 S, 16.7 to 5000 S and 33.3 to 10 000 S, respectively (see Tables 1 and 2). The same values can be obtained for current flow in the east–west direction. Note that we have considered test magma bodies with conductances greater than and less than the 300 S conductance of C1.

We use two methods to quantify whether or not the edited resistivity model differs from the preferred inversion model: the Kolmogorov–Smirnov (K–S) test and the change in r.m.s. misfit. The two sample K–S test is a non-parametric hypothesis test that determines whether two populations are from the same continuous distribution within some significance level (Massey Jr 1951; Miller & Kahn 1962). If the asymptotic significance, or p-value, is larger than the significance level, then we accept the null hypothesis that the two populations are from the same distribution. A p-value less than the significance level is statistically significant and indicates that the null hypothesis can be rejected and the distributions are different.

We perform the K–S test with the function *kstest2* in MATLAB (The MathWorks, Inc. 2016). The test considers two populations x_1 and x_2, with n_1 and n_2 samples, respectively. Let D represent the maximum difference between their empirical distribution functions, F_1 and F_2. If D is greater than some critical value, then the null hypothesis is rejected. Instead of computing the critical value, *kstest2* accepts or rejects the null hypothesis by computing the asymptotic p-value and comparing it with the significance level.

In these resolution tests we are interested in whether or not the MT data are sensitive to the added anomalies in the edited models. We compare the residuals (normalized by error) from the original model to the residuals (normalized by error) of the calculated response of the edited model. In our case, the two populations x_1 and x_2 are the two sets of normalized residuals. If the null hypothesis is accepted (p-value greater than significance level), then we cannot conclusively determine if the two sets of residuals are drawn from the same or different distributions. If the null hypothesis is rejected (p-value less than significance level), we conclude that the two sets of residuals are distinct and thus the added anomaly has a statistically significant impact on the inversion response. We determined if the change in the MT data is statistically significant by comparing the MT data residuals (normalized by error) of each model. We will consider the anomaly in the edited model as 'detected' by the MT data if the K–S tests returns a statistically significant p-value (null hypothesis is rejected). It should be emphasized that the significance level is arbitrary and does not influence the calculated p-value. In this paper we used a significance level of 0.05 for all K–S tests.

The change in r.m.s. misfit between an inversion model and an edited model has also been used to assess the sensitivity of MT data to a test anomaly (e.g. Hill *et al.* 2009; Cordell *et al.* 2018). While an increase or decrease in r.m.s. misfit suggests that the MT data are sensitive to a test anomaly, the threshold of detection is somewhat arbitrary and it is unclear how large of a change in r.m.s misfit is significant. In addition, because the r.m.s. misfit is calculated from squared residuals, it only represents a relative difference between the two sets of residuals (i.e. no information on positive or negative bias). The K–S test has the benefit of giving a summary statistic that is sensitive to a positive or negative difference between residuals. A third method to assess sensitivity follows the method of Piña–Varas *et al.* (2018). They added test magma bodies to their resistivity model of the Teide volcano and calculated the per cent change in apparent resistivity. The MT data were considered to be sensitive to the test anomaly if the change in apparent resistivity was greater than the error floor used in the MT inversion. We use the same approach to consider if the MT data are sensitive to an added anomaly. This method is visually helpful to identify data points with large changes but does not provide a summary statistic for the data set as a whole.

Resolution test: thin sill (B1)

The first test (B1) modelled a thin sill of magma located at a depth of 1.6 km. The sill extends 3 km in the north–south and east–west directions, and has a thickness of 0.25 km. In the first test the sill has a resistivity of 30 Ωm (conductance of 8.3 S), which is the upper end of the resistivity range calculated in the previous section. Table 2 shows the change in r.m.s. misfit from the inversion model when the sill is assigned the chosen resistivity value. The r.m.s. misfit changes by less than 0.01 when the 30, 10 and 3 Ωm sills are added to the model. These sills have conductances of 8.3, 25 and 83 S, respectively. It is also useful to examine changes at individual stations because overall r.m.s. misfit considers the entire data set. In general, stations close to the sill such as KMT50 (0.4 km from IDDP-1) exhibit larger changes in their data. Fig. 16 shows the off-diagonal apparent resistivity and phase curves for station KMT50

Downloaded from https://academic.oup.com/gji/article/220/1/541/5587733 by guest on 30 March 2022

Table 1. *P*-values returned by K–S tests of the 18 sensitivity tests. Statistically significant *p*-values were obtained for the 0.1 and 0.3 Ωm sills.

p-values for test magma bodies, alpha = 0.05				
Resistivity (Ωm)	Conductance (S) B1, B2, B3	B1: Thin sill 3 km × 3 km × 0.25 km	B2: Small cube 0.5 km × 0.5 km × 0.5 km	B3: Large cube 1 km × 1 km × 1 km
30	8.3, 16.7, 33.3	1	1	1
10	25, 50, 100	1	1	1
3	83, 167, 333	1	1	1
1	250, 500, 1000	8.2E−1	1	1
0.3	833, 1667, 3333	6.1E−3	1	1
0.1	2500, 5000, 10 000	1.3E−5	1	1

Table 2. Change in r.m.s. misfit when the inversion resistivity model is edited. Note that a value of 0 indicates a change in r.m.s. misfit less than 0.01.

r.m.s. misfit change for test magma bodies (inversion r.m.s. misfit = 1.04)				
Resistivity (Ωm)	Conductance (S) B1, B2, B3	B1: Thin sill 3 × km × 3 km × 0.25 km	B2: Small cube 0.5 km × 0.5 km × 0.5 km	B3: Large cube 1 km × 1 km × 1 km
30	8.3, 16.7, 33.3	0	0	0
10	25, 50, 100	0	0	0
3	83, 167, 333	0	0	0
1	250, 500, 1000	0.02	0	0
0.3	833, 1667, 3333	0.08	0	0
0.1	2500, 5000, 10 000	0.15	0	0

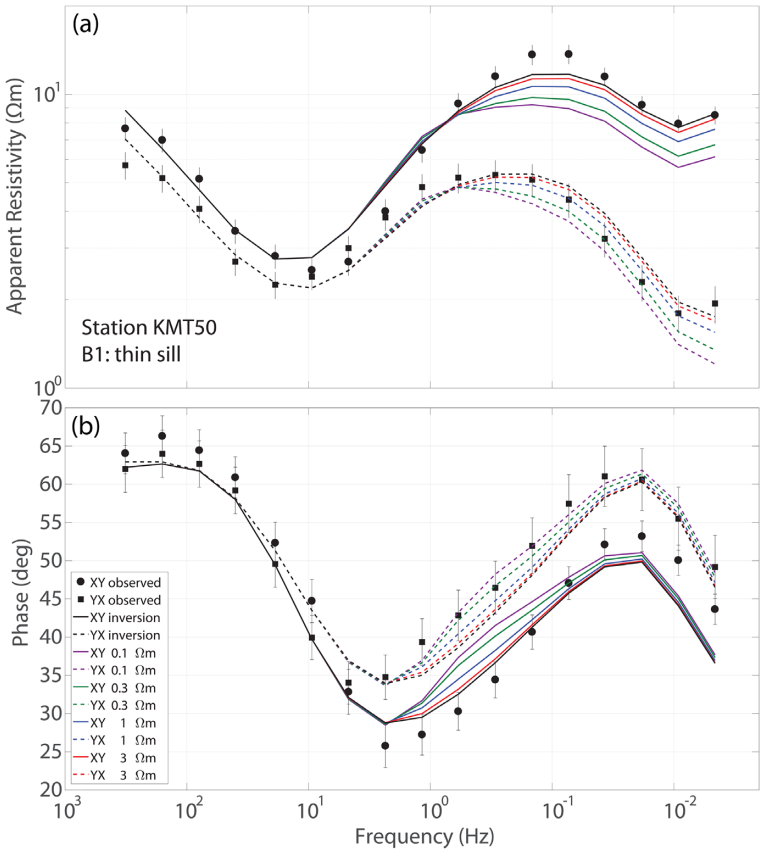

Figure 16. (a) Apparent resistivity and (b) phase curves as functions of period for the station KMT50. The circles and squares are the observed MT data, and the black lines are the calculated inversion response. The coloured lines are the calculated data for synthetic sills added to the inversion resistivity model. See figure legend for symbol definitions. Note that the 10 and 30 Ωm sill responses are omitted because they are nearly coincident with the inversion response.

when the test sills are edited into the model. Fig. 16 also shows the observed and calculated inversion data for comparison. This is a qualitative way to examine the change in MT data at one station. As expected, the 0.1 Ωm sill causes the largest change in the apparent resistivity and phase data. The more resistive 10 and 30 Ωm sills do not cause much of a change from the calculated inversion data and are not plotted in Fig. 16 because they overlap the inversion response.

Downloaded from https://academic.oup.com/gji/article/220/1/541/5587733 by guest on 30 March 2022

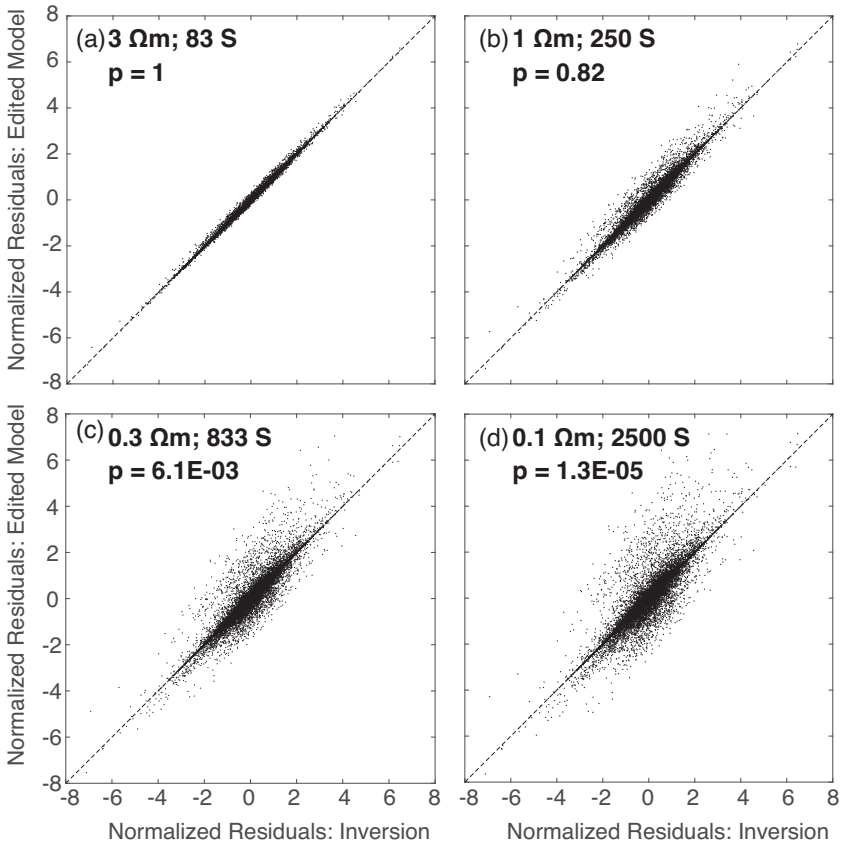

Figure 17. Cross-plot of impedance residuals for the unconstrained inversion and the edited model with (a) 3 Ωm (83 S) sill, (b) 1 Ωm (250 S) sill, (c) 0.3 Ωm (833 S) sill, and (d) 0.1 Ωm (2500 S) sill. In (a) and (b) the impedance residuals for both models plot close to the 1-to-1 line (dashed line) and the K–S test returns a statistically insignificant p-value with alpha = 0.05. When the impedance residuals of both models show a large difference as in (c) and (d), the p-value is statistically significant.

We can examine trends in the entire MT data set in order to assess if the data are sensitive to the synthetic sills. Fig. 17 shows a cross-plot of the normalized impedance data residuals for the 3, 1, 0.3 and 0.1 Ωm (83, 250, 833, 2500 S) sills. The cross-plot is a qualitative way to examine the difference between the two sets of data residuals. In each panel, the residuals for every station and all eight components of the complex impedance are shown. If the residuals from the inversion and the edited model response are exactly the same, they will plot on the dashed 1-to-1 line. In this case, the addition of the 3 Ωm sill does not move the plotted impedance residuals appreciably from the 1-to-1 line. In fact, the K–S test returns a p-value of 1 and the change in misfit between the two models is less than 0.01. We can conclude that the MT data fit is not appreciably changed when the 3 Ωm sill is added to the model. When the resistivity of the sill is decreased to 1, 0.3 and 0.1 Ωm (250, 833, 2500 S), the K–S test returns p-values less than 1, and the changes in r.m.s. misfit are greater than 0.01. In these cases it is apparent that the MT data for the inversion and edited models are different . In particular, the 0.3 and 0.1 Ωm sills are detected by the MT data because the corresponding p-values are lower than the significance level of 0.05.

The r.m.s. misfit increases the most (0.15) with the 0.1 Ωm sill. However, in this case the r.m.s. misfit is still rather low (1.19), which could subjectively be considered as an acceptable fit to the observed MT data. The p-value returned by the K–S test is 1.3E−05, which is far below the significance level of 0.05. This suggests that the data residuals from the inversion model and edited model can be considered to be drawn from two different distributions, and thus the two models are different enough for a change in data to be detected. This also highlights why a small change in r.m.s. misfit alone is not sufficient to determine whether two data sets are different in a significant way. The change in impedance residuals, shown in Fig. 18, also supports this conclusion. Fig. 18 shows the normalized change in each impedance component for every station and period between the inversion model and the model with the 0.1 Ωm sill. Values between 0 and 1 correspond to changes smaller than the imposed error floor and are plotted in white to emphasize changes larger than the error floor. Many stations show a normalized difference greater than 1 for intermediate and long periods, which suggests that these data are sensitive to the addition of the 0.1 Ωm sill despite a relatively small change in overall r.m.s. misfit. Note that the normalized differences are greater for the off-diagonal components (Z_{xy} and Z_{yx}) than the diagonal components (Z_{xx} and Z_{yy}) due to the fact that the same error floor was applied to all components, and the diagonal components are one to two orders of magnitude smaller than the off-diagonal components. Fig. 19 shows the p-values for each station when comparing the inversion model and the model with the 0.1 Ωm sill. Most of the stations with a statistically significant difference in residuals are located directly above the sill. Note that several stations did not contain data >50 s and are shown as a grey circle in Fig. 19. Stations located above the southeastern corner of the sill show a high p-value, suggesting that they would not be sensitive to the presence of the sill. Conversely, some stations that are not located directly above the sill have statistically significant

Downloaded from https://academic.oup.com/gji/article/220/1/541/5587733 by guest on 30 March 2022

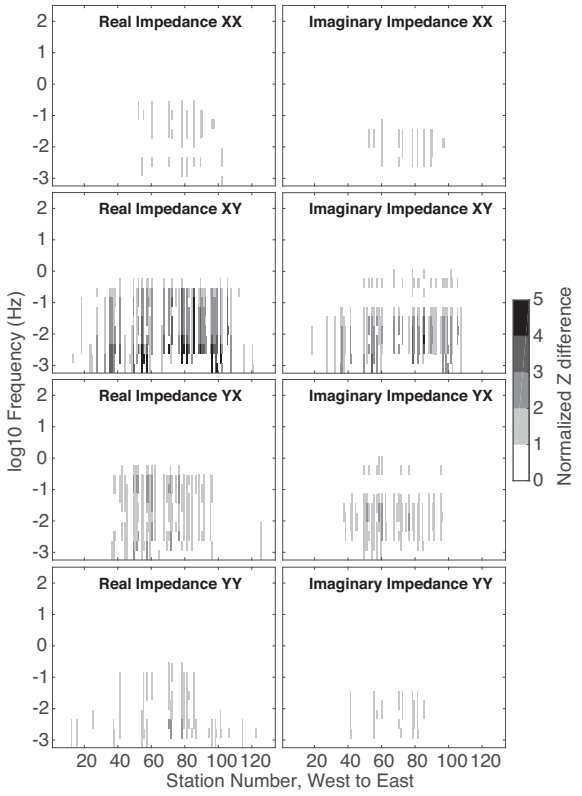

Figure 18. Difference in impedance normalized by error floor for the forward modelling test with a 0.1 Ωm (2500 S) sill (B1).

p-values. We believe this is because the *p*-value depends on several factors such as the resistivity model recovered by the inversion, the fit of the predicted data and the distance to the sill.

We would expect stations located above the highly conductive clay layer to have a diminished resolution towards any deeper conductors. This is likely due to the fact that the 1-D conductance is a simple approximation that does not accurately represent the current flow in all parts of a 3-D model. The true conductance will be different from the 1-D conductance when conductivity varies in the horizontal *x*- and *y*-directions. However, the test sills underlie a significant area below Krafla and are relatively 1-D compared to the cubic test magma bodies. As predicted in Section 5.1, a conductor below C1 would need a conductance greater than 300 S to be detected by the MT data. The results from the test sills support this idea, as only the sills with conductances greater than that of C1 (833 and 2500 S) produced statistically significant *p*-values and appreciable changes in r.m.s. misfit.

Resolution test: cubic magma bodies (B2 and B3)

We also tested if the MT data were sensitive to hypothetical cubic magma bodies at the same location as the sill. The small test cube (B2) had dimensions of 0.5 km × 0.5 km × 0.5 km while the large cube had dimensions of 1 km × 1 km × 1 km (see Fig. 15 for locations). As seen in Tables 1 and 2, the small and large cubes were not detected for the tested resistivities. The r.m.s. misfit remained at 1.04 when the small and large cubes were edited into the model with resistivities of 30, 10, 3, 1, 0.3 and 0.1 Ωm. In addition, the K–S test returned a statistically insignificant *p*-value of 1 for each test with the small and large cubes. Thus, editing the model to include even a 1 km^3 conductive magma body does not produce an appreciable change in the MT data, implying that the MT data are insensitive to a small intrusion at the bottom of the IDDP-1 well.

Out of our 18 resolution tests we found that the MT data are only sensitive to the presence of the 0.3 and 0.1 Ωm sills. Even though the sill was only 0.25 km thick compared to the 0.5 and 1 km thick cubes, the resolution tests showed that the 0.3 and 0.1 Ωm (833 and 2500 S) sills would be easily detected by the MT data, while the 0.3 and 0.1 Ωm (3333 and 10 000 S) cubes would be undetected. This seems to contradict the idea that anomalies of higher conductance would be more easily detected by MT data. Though the large cube has a conductance four times greater than the sill, it is not at all detected by the MT data. This suggests that the volume distribution of conductivity is also important in determining whether or not MT data are sensitive to the presence of a 3-D anomaly.

It is important to note that the test sill is larger than the expected size of rhyolite intrusions below Krafla. For example, silicic glass was recovered from the cuttings of well K-39, which suggests that the well intersected a thin sill on the order of 1–10 m thick (Mortensen *et al.* 2010). We did not add a 10 m thick sill to a depth of 1.6 km b.s.l. in the model because this is well below the expected spatial resolution of the MT method at such a depth. In addition, because the inversion is more stable when neighbouring cells are a similar size (no more than ∼1.5 times larger) it would not be computationally feasible to include such thin cells at such a depth in the model.

7 CONCLUSIONS

We have re-examined the MT data at the Krafla geothermal field in order to understand why the IDDP-1 well unexpectedly drilled into rhyolite magma at 1.6 km b.s.l. With a new 3-D MT inversion and resolution tests, we have addressed three possible reasons why the magma body was initially undetected:

(1) The location of the rhyolitic magma directly beneath a highly conductive clay layer makes it difficult to be resolved with the MT method;
(2) The rhyolitic magma body intersected by IDDP-1 has a relatively high resistivity that does not present itself as an obvious anomaly in the resistivity model.
(3) The magma body was not detected due to limitations of the 1-D inversion.

(1) The Krafla geothermal field contains a clay layer about 0.5 km thick. We have shown that the 1-D conductance of the clay layer exceeds 300 S locally which limits the resolution of deeper low resistivity features. We edited test magma bodies into our inversion resistivity model in order to assess the MT data resolution. Our resolution tests with a sill and two magma cubes tested the maximum resistivity that would produce a statistically significant difference in the MT data. The MT data only showed a statistically significant difference when the 0.3 Ωm (833 S) and 0.1 Ωm (2500 S) sills (3 km × 3 km × 0.25 km) were added to the model. Out of the six test sills, only the sills with conductance greater than C1 (300 S) were detected by the MT data. These sills are much less resistive than our predicted range of 0.7 to 30 Ωm. This implies that the MT data would have detected these sills if one existed at this depth, and that the observed MT data do not support the existence of a thin sill at a depth of 1.6 km b.s.l.. The 3 and 1 Ωm sills did not produce a large change in r.m.s. misfit or statistically significant *p*-values; thus we cannot preclude the existence of one of these sills based on

Downloaded from https://academic.oup.com/gji/article/220/1/541/5587733 by guest on 30 March 2022

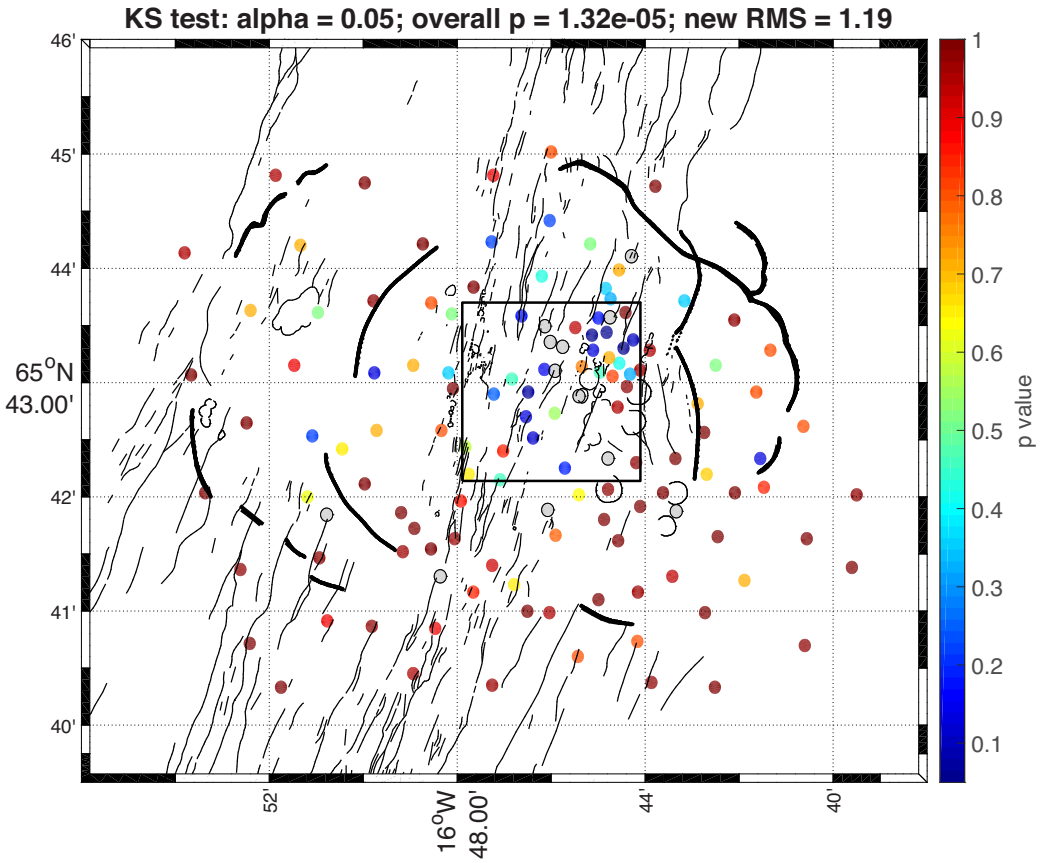

Figure 19. Asymptotic *p*-values returned by the K–S test at each MT station when comparing impedance residuals of the inversion model and model with a 0.1 Ωm (2500 S) sill. Grey circles = MT stations with no data above 50 s. The black box shows the outline of the sill.

these resolution tests alone. However, wells within 1 km of IDDP-1 and of similar depth such as K10 (1.515 km b.s.l.), K11 (1.720 km) and K25 (1.555 km) did not intersect magma. Clearly the sill model is too simplistic and the actual distribution of intrusions varies on a spatial scale that is not resolvable by the MT data at this depth. The small magma cubes (0.125 and 1 km^3) were also undetected by the MT data when considering overall r.m.s. misfit and the two-sample KS test. Although these cubes have conductances as high as 10 000 S, it is clear that they are too small to affect the overall bulk resistivity at a depth of 1.6 km b.s.l.

(2) Using available petrological and laboratory melt data, we estimate that for a large range of melt fractions (0.1 to 0.9) the Krafla rhyolite could have a bulk resistivity of 0.7 to 30 Ωm. This is relatively high compared to the resistivity of silicic magma reservoirs in the Taupo Volcanic Zone, New Zealand and the Laguna del Maule volcanic field, Chile. Although the IDDP-1 rhyolite is located in a low resistivity region of our resistivity model (∼ 7 Ωm), the low resistivity can be due to several factors. From the resolution tests we can conclude that the magma body would only be detected if it was a large 0.1 or 0.3 Ωm sill. However, it is clear that resistivity is not the only factor in detection because the MT data were insensitive to smaller magma bodies of 0.1 and 0.3 Ωm resistivity. Thus we cannot conclusively determine if the rhyolite was undetected due to a relatively high resistivity. Future tests could involve more realistically shaped magma bodies to reflect the complex distribution of melt below Krafla.

(3) The location and geometry of the deep conductor C3 was different in our 3-D resistivity model compared to the 1-D resistivity model of Árnason *et al.* (2008). A 1-D inversion is an approximation that may not be accurate in complex geological settings. The MT phase tensor data show evidence for 3-D structures at intermediate frequencies, which indicates that 3-D inversion is more appropriate. However, with respect to points (1) and (2), even the 3-D inversion has limited sensitivity to the IDDP-1 rhyolite. The 3-D inversion provides a more accurate resistivity model than the 1-D inversion, but limited resolution to deep conductors is a general limitation of the MT method.

Our new 3-D resistivity model includes features that agree well with observed alteration and mineralogy from drill cuttings. The shallow clay layer contains high-CEC smectite and zeolite, and appears as a low resistivity feature in the upper 0.3 km of the model. The chlorite–epidote core beneath the Vitismor and Leirbotnar fields is a resistive feature in contrast to a conductive zone immediately to the east, associated with aqueous fluids within the Hveragil fault system and a major feed zone beneath Sudurhlidar. A large, low resistivity feature (C3) is present beneath the northern inner caldera at a depth of about 2 km b.s.l. We believe there are two possible interpretations for this feature: (1) a zone of partial melt, or (2) a zone of dehydrated chlorite and epidote alteration minerals. The possibility of partial melt is not clearly supported by seismic velocity and observed shear wave attenuation. With respect to dehydrated chlorite and epidote, recent laboratory melt studies show that when heated above 500 °C, chlorite and epidote release aqueous fluids that significantly decrease electrical resistivity. Chlorite decomposition also leads to the formation of interconnected magnetite, further

Downloaded from https://academic.oup.com/gji/article/220/1/541/5587733 by guest on 30 March 2022

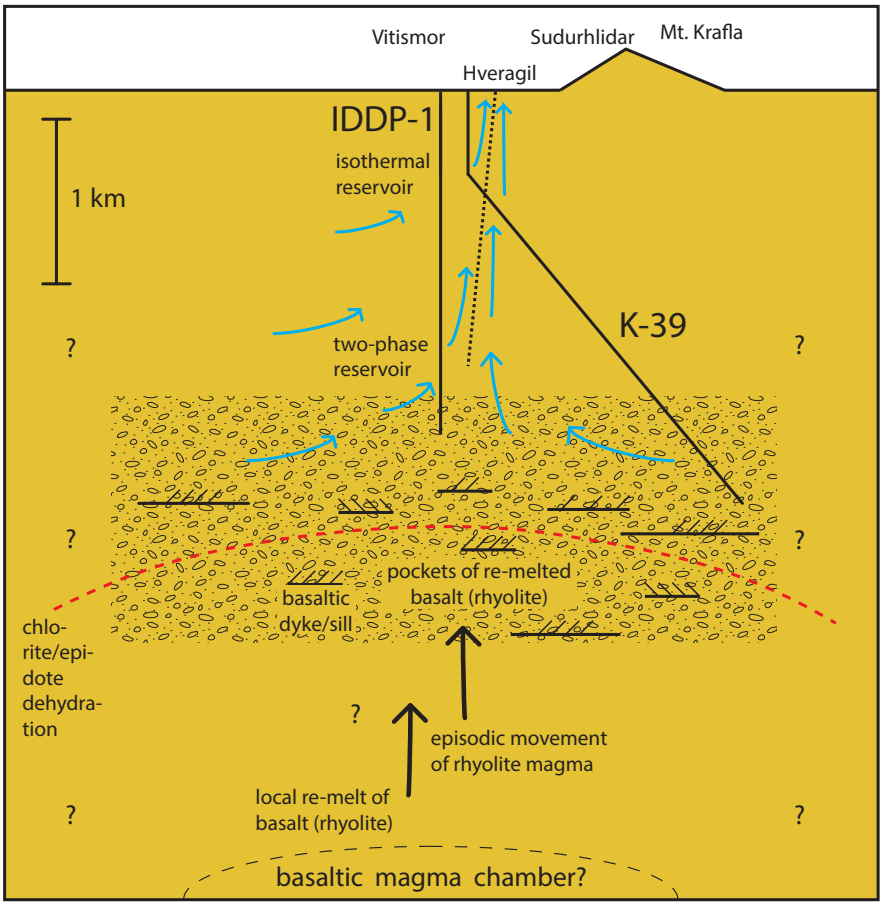

Figure 20. Conceptual west-to-east cross-section model of the Krafla geothermal system and underlying magmatic system. Blue arrows: fluid flow based on hydrogeological model of Pope et al. (2016).

decreasing electrical resistivity (Manthilake *et al.* 2016). Low resistivity zones observed beneath the Hengill and Námafjall geothermal fields in Iceland have also been linked to dehydration of alteration minerals (Nono *et al.* 2018). However, our resolution tests suggest that the MT data do not have the ability to differentiate between small magma bodies that are periodically intruded into shallow depths beneath Krafla.

A conceptual model of the Krafla geothermal field and the underlying magmatic system is illustrated in Fig. 20. The IDDP-1 and K-39 wells intersected rhyolite magma at 1.6 and 2.1 km b.s.l., respectively. These are shallower than the ∼3 km depth to a deep magma chamber first predicted by Einarsson (1978). Analysis of Krafla rhyolites suggests a component of re-melted, hydrothermally altered basalt (Jónasson 1994; Jónasson 2007; Elders *et al.* 2011; Zierenberg *et al.* 2013). These may exist as local pockets of rhyolite melt below Krafla. Above 500 to 600 °C chlorite and epidote alteration minerals are dehydrated and lead to a decrease in resistivity as water is released and magnetite is formed (red dashed line in Fig. 20).

This study has implications for interpretation of features, particularly conductors, in volcanic geothermal settings. A shallow clay layer is a common feature of volcanic systems that experienced low-temperature (100 to 220 °C) hydrothermal alteration. We have shown limited resolution to magma intrusions that are located beneath the clay layer. The Krafla MT data were only sensitive to the synthetic sill at 1.6 km b.s.l. when the sill was unrealistically large and the resistivity was at the lower end of the range predicted from petrological and laboratory melt data. Thus, resolution tests should be performed before interpretation of conductors beneath a shallow clay layer.

ACKNOWLEDGEMENTS

We would like to thank Landsvirkjun, the National Power Company in Iceland, for making the magnetotelluric data available. We would also like to thank two anonymous reviewers for their comments that improved the manuscript. Thanks to Gary Egbert, Anna Kelbert and Naser Meqbel for providing their ModEM inversion program. This research was undertaken thanks in part to funding from the Canada First Research Excellence Fund and a NSERC Discovery Grant to MU. Computational resources were provided by Westgrid and Compute Canada.

REFERENCES

Allen, R.M., Nolet, G., Morgan, W.J., Vogfjörd, K., Bergsson, B.H., Erlendsson, P. & Ragnarsson, S., 1999. The thin hot plume beneath Iceland, *Geophys. J. Int.,* **137**(1), 51–63.

Árnason, K., Karlsdottir, R., Eysteinsson, H., Flóvenz, Ó.G. & Gudlaugsson, S.T., 2000. The resistivity structure of high-temperature geothermal systems in Iceland, in *Proceedings of the World Geothermal Congress 2000,* Kyushu-Tohoku, Japan, pp. 923–928.

Downloaded from https://academic.oup.com/gji/article/220/1/541/5587733 by guest on 30 March 2022

Árnason, K., Vilhjálmsson, A.M. & Björnsdóttir, Þ., 2008. A study of the Krafla volcano using gravity, micro-earthquake and MT data, in *Interim ISOR Report to Landsvirkjun,* Lake Naivasha, Kenya, pp. 1–14.

Árnason, K., Eysteinsson, H. & Hersir, G.P., 2010. Joint 1D inversion of TEM and MT data and 3D inversion of MT data in the Hengill area, SW Iceland, *Geothermics,* **39**(1), 13–34.

Arnott, S.K. & Foulger, G.R., 1994. The Krafla spreading segment, Iceland: 1. Three-dimensional crustal structure and the spatial and temporal distribution of local earthquakes, *J. geophys. Res.,* **99**(B12), 23 801–23 825.

Avdeeva, A., Moorkamp, M., Avdeev, D., Jegen, M. & Miensopust, M., 2015. Three-dimensional inversion of magnetotelluric impedance tensor data and full distortion matrix, *Geophys. J. Int.,* **202**(1), 464–481.

Axelsson, G., Egilson, T. & Gylfadóttir, S.S., 2014. Modelling of temperature conditions near the bottom of well IDDP-1 in Krafla, Northeast Iceland, *Geothermics,* **49,** 49–57.

Bahr, K., 1988. Interpretation of the magnetotelluric impedance tensor: regional induction and local telluric distortion, *J. Geophys,* **62**(2), 119–127.

Bai, D., Unsworth, M.J., Meju, M.A., Ma, X., Teng, J., Kong, X. & Zhao, C., 2010. Crustal deformation of the eastern Tibetan plateau revealed by magnetotelluric imaging, *Nat. Geosci.,* **3**(5), 358–362.

Becken, M., Ritter, O., Park, S.K., Bedrosian, P.A., Weckmann, U. & Weber, M., 2008. A deep crustal fluid channel into the San Andreas Fault system near Parkfield, California, *Geophys. J. Int.,* **173**(2), 718–732.

Bibby, H.M., Risk, G.F., Caldwell, T.G. & Heise, W., 2009. Investigations of deep resistivity structures at the Wairakei geothermal field, *Geothermics,* **38**(1), 98–107.

Bjornsson, A., Eysteinsson, H. & Beblo, M., 2005. Crustal formation and magma genesis beneath Iceland: magnetotelluric constraints, *Special Papers Geol. Soc. Am.,* **388,** 665–686.

Booker, J.R., 2014. The magnetotelluric phase tensor: a critical review, *Surv. Geophys.,* **35**(1), 7–40.

Brandsdóttir, B., Menke, W., Einarsson, P., White, R.S. & Staples, R.K., 1997. Färoe-Iceland Ridge Experiment 2. Crustal structure of the Krafla central volcano, *J. geophys. Res.,* **102**(B4), 7867–7886.

Caldwell, T.G., Bibby, H.M. & Brown, C., 2004. The magnetotelluric phase tensor, *Geophys. J. Int.,* **158**(2), 457–469.

Campanyà, J., Ledo, J., Queralt, P., Marcuello, A., Muñoz, J.A., Liesa, M. & Jones, A.G., 2018. New geoelectrical characterization of a continental collision zone in the central–eastern Pyrenees: Constraints from 3-D joint inversion of electromagnetic data, *Tectonophysics,* **742,** 168–179.

Cordell, D., Unsworth, M.J. & Díaz, D., 2018. Imaging the Laguna del Maule Volcanic Field, central Chile using magnetotellurics: Evidence for crustal melt regions laterally-offset from surface vents and lava flows, *Earth planet. Sci. Lett.,* **488,** 168–180.

Cumming, W. & Mackie, R., 2010. Resistivity imaging of geothermal resources using 1D, 2D and 3D MT inversion and TDEM static shift correction illustrated by a Glass Mountain case history, in *Proceedings World Geothermal Congress,* Indonesia, Bali, pp. 25–29.

DeMets, C., Gordon, R.G., Argus, D.F. & Stein, S., 1990. Current plate motions, *Geophys. J. Int.,* **101**(2), 425–478.

Einarsson, P., 1978. S-wave shadows in the Krafla caldera in NE-Iceland, evidence for a magma chamber in the crust, *Bull. Volcanol.,* **41**(3), 187–195.

Elders, W.A., Friðleifsson, G.Ó., Zierenberg, R.A., Pope, E.C., Mortensen, A.K., Guðmundsson, Á. & Reed, M., 2011. Origin of a rhyolite that intruded a geothermal well while drilling at the Krafla volcano, Iceland, *Geology,* **39**(3), 231–234.

Elders, W.A., Friðleifsson, G.Ó. & Albertsson, A., 2014. Drilling into magma and the implications of the Iceland Deep Drilling Project (IDDP) for high-temperature geothermal systems worldwide, *Geothermics,* **49,** 111–118.

Flóvenz, Ó.G. & Gunnarsson, K., 1991. Seismic crustal structure in Iceland and surrounding area, *Tectonophysics,* **189**(1-4), 1–17.

Flóvenz, Ó.G. & Saemundsson, K., 1993. Heat flow and geothermal processes in Iceland, *Tectonophysics,* **225**(1-2), 123–138.

Fridleifsson, G.O., 2003. Iceland Deep Drilling Projectfeasibility report, *Iceland Energy Authority,* Orkustofnun Report OS-2003-007.

Fridleifsson, G.O. & Elders, W.A., 2005. The Iceland Deep Drilling Project: a search for deep unconventional geothermal resources, *Geothermics,* **34**(3), 269–285.

Fridleifsson, G.O., Ármannsson, H., Guðmundsson, Á., Árnason, K., Mortensen, A.K., Pálsson, B. & Einarsson, G.M., 2014. Site selection for the well IDDP-1 at Krafla, *Geothermics,* **49,** 9–15.

Fridleifsson, G.O., Elders, W.A., Zierenberg, R.A., Stefánsson, A., Fowler, A.P., Weisenberger, T.B. & Mesfin, K.G., 2017. The Iceland Deep Drilling Project 4.5 km deep well, IDDP-2, in the seawater-recharged Reykjanes geothermal field in SW Iceland has successfully reached its supercritical target, *Sci. Drill.,* **23,** 1, doi:0.5194/sd-23-1-2017.

Foulger, G.R. & Anderson, D.L., 2005. A cool model for the Iceland hotspot, *J. Volc. Geotherm. Res.,* **141**(1), 1–22.

Gasperikova, E., Rosenkjaer, G.K., Árnason, K., Newman, G.A. & Lindsey, N.J., 2015. Resistivity characterization of the Krafla and Hengill geothermal fields through 3D MT inverse modeling, *Geothermics,* **57,** 246–257.

Gibert, B., Levy, L., Sigmundsson, F., Hersir, G.P. & Flovenz, Ó.G., 2017. *Electrical conductivity of basaltic and rhyolitic melts from Krafla central volcano, Iceland*. Abstract submitted to the IMAGE Final Conference, Akureyri, Iceland. 4–6 Oct. 2017)

Glover, P.W., Hole, M.J. & Pous, J., 2000. A modified Archie's law for two conducting phases, *Earth planet. Sci. Lett.,* **180**(3), 369–383.

Groom, R.W. & Bailey, R.C., 1989. Decomposition of magnetotelluric impedance tensors in the presence of local three-dimensional galvanic distortion, *J. geophys. Res.,* **94**(B2), 1913–1925.

Gudmundsson, A., 1998. Magma chambers modeled as cavities explain the formation of rift zone central volcanoes and their eruption and intrusion statistics, *J. geophys. Res.,* **103**(B4), 7401–7412.

Guo, X., Zhang, L., Behrens, H. & Ni, H., 2016. Probing the status of felsic magma reservoirs: Constraints from the P–T–H2O dependences of electrical conductivity of rhyolitic melt, *Earth planet. Sci. Lett.,* **433,** 54–62.

Heise, W., Caldwell, T.G., Bibby, H.M. & Bennie, S.L., 2010. Three-dimensional electrical resistivity image of magma beneath an active continental rift, Taupo Volcanic Zone, New Zealand, *Geophys. Res. Lett.,* **37**(10).

Hill, G.J., Caldwell, T.G., Heise, W., Chertkoff, D.G., Bibby, H.M., Burgess, M.K. & Cas, R.A., 2009. Distribution of melt beneath Mount St Helens and Mount Adams inferred from magnetotelluric data, *Nat. Geosci.,* **2**(11), 785–789.

Hu, H., Dai, L., Li, H., Hui, K. & Sun, W., 2017. Influence of dehydration on the electrical conductivity of epidote and implications for high-conductivity anomalies in subduction zones, *J. geophys. Res.,* **122**(4), 2751–2762.

Jónasson, K., 1994. Rhyolite volcanism in the Krafla central volcano, northeast Iceland, *Bull. Volcanol.,* **56**(6-7), 516–528.

Jónasson, K., 2007. Silicic volcanism in Iceland: composition and distribution within the active volcanic zones, *J. Geodyn.,* **43**(1), 101–117.

Karlsdóttir, R., Vilhjálmsson, A.M. & Teklesenbet, A., 2015. Námafjall high temperature field in N Iceland. A 3D resistivity model derived from MT data, in *Proceedings of the 2015 World Geothermal Congress,* Melbourne, Australia, pp. 1–7.

Kelbert, A., Meqbel, N., Egbert, G.D. & Tandon, K., 2014. ModEM: A modular system for inversion of electromagnetic geophysical data, *Comput. Geosci.,* **66,** 40–53.

Kim, D., Brown, L.D., Árnason, K., Águstsson, K. & Blanck, H., 2017. Magma reflection imaging in Krafla, Iceland, using microearthquake sources, *J. geophys. Res.,* **122,** 5228–5242.

Kiyan, D., Jones, A.G. & Vozar, J., 2013. The inability of magnetotelluric off-diagonal impedance tensor elements to sense oblique conductors in three-dimensional inversion, *Geophys. J. Int.,* **196**(3), 1351–1364.

Levy, L., 2019. Electrical properties of hydrothermally altered rocks: observations and interpretations based on laboratory, field and borehole studies at Krafla volcano, Iceland, *PhD thesis at PSL University, Paris and University of Iceland*. Available online at https://hdl.handle.net/20.500.11815/1140

Downloaded from https://academic.oup.com/gji/article/220/1/541/5587733 by guest on 30 March 2022

Lindsey, N.J. & Newman, G.A., 2015. Improved workflow for 3D inverse modeling of magnetotelluric data: Examples from five geothermal systems, *Geothermics,* **53,** 527–532.

Manthilake, G., Bolfan-Casanova, N., Novella, D., Mookherjee, M. & Andrault, D., 2016. Dehydration of chlorite explains anomalously high electrical conductivity in the mantle wedges, *Sci. adv.,* **2**(5), e1501631.

Massey, F.J., Jr., 1951. The Kolmogorov-Smirnov test for goodness of fit, *J. Am. Stat. Assoc.,* **46**(253), 68–78.

Miensopust, M.P., 2017. Application of 3-D Electromagnetic Inversion in Practice: Challenges, Pitfalls and Solution Approaches, *Surv. Geophys.,* **38**(5), 869–933.

Miller, R.L. & Kahn, J.S., 1962. *Statistical Analysis in the Geological Sciences,* Wiley.

Mortensen, A.K., Grönvold, K., Gudmundsson, Á., Steingrímsson, B. & Egilson, T., 2010. Quenched silicic glass from well K-39 in Krafla, North-Eastern Iceland, in *World Geothermal Congress,* Bali, Indonesia, pp. 1–6.

Mortensen, A.K., Egilson, Þ., Gautason, B., Árnadóttir, S. & Guðmundsson, Á.., 2014. Stratigraphy, alteration mineralogy, permeability and temperature conditions of well IDDP-1, Krafla, NE-Iceland, *Geothermics,* **49,** 31–41.

Newman, G.A., Gasperikova, E., Hoversten, G.M. & Wannamaker, P.E., 2008. Three-dimensional magnetotelluric characterization of the Coso geothermal field, *Geothermics,* **37**(4), 369–399.

Nono, F., Gibert, B., Parat, F., Loggia, D., Cichy, S.B. & Violay, M., 2018. Electrical conductivity of Icelandic deep geothermal reservoirs up to supercritical conditions: Insight from laboratory experiments, *J. Volc. Geotherm. Res*.

Onacha, S.A., 2006. *Hydrothermal fault zone mapping using seismic and electrical measurements* (Order No. 3267808). Available From ProQuest Dissertations & Theses Global. (305325409).

Patro, P.K. & Egbert, G.D., 2011. Application of 3D inversion to magnetotelluric profile data from the Deccan Volcanic Province of Western India, *Phys. Earth planet. Inter.,* **187**(1-2), 33–46.

Piña-Varas, P., Ledo, J., Queralt, P., Marcuello, A. & Perez, N., 2018. On the detectability of Teide volcano magma chambers (Tenerife, Canary Islands) with magnetotelluric data, *Earth Planet Space,* **70**(1), 14.

Pope, E.C., Bird, D.K., Arnorsson, S. & Giroud, N., 2016. Hydrogeology of the Krafla geothermal system, northeast Iceland, *Geofluids,* **16**(1), 175–197.

Rosenberg, C.L. & Handy, M.R., 2005. Experimental deformation of partially melted granite revisited: implications for the continental crust, *J. Metamorph. Geol.,* **23**(1), 19–28.

Rosenkjaer, G.K., Gasperikova, E., Newman, G.A., Árnason, K. & Lindsey, N.J., 2015. Comparison of 3D MT inversions for geothermal exploration: Case studies for Krafla and Hengill geothermal systems in Iceland, *Geothermics,* **57,** 258–274.

Sasaki, Y. & Meju, M.A., 2006. Three-dimensional joint inversion for magnetotelluric resistivity and static shift distributions in complex media, *J. geophys. Res.,* **111**(B5).

Schuler, J., Greenfield, T., White, R.S., Roecker, S.W., Brandsdóttir, B., Stock, J.M. & Pugh, D., 2015. Seismic imaging of the shallow crust beneath the Krafla central volcano, NE Iceland, *J. geophys. Res.,* **120**(10), 7156–7173.

Scott, S., Driesner, T. & Weis, P., 2015. Geologic controls on supercritical geothermal resources above magmatic intrusions, *Nat. Commun.,* **6,** 7837, doi:10.1038/ncomms8837.

Sigmarsson, O., Hémond, C., Condomines, M., Fourcade, S. & Oskarsson, N., 1991. Origin of silicic magma in Iceland revealed by Th isotopes, *Geology,* **19**(6), 621–624.

Simpson, F. & Bahr, K., 2005. *Practical Magnetotellurics*. Cambridge University Press.

Siripunvaraporn, W., 2012. Three-dimensional magnetotelluric inversion: an introductory guide for developers and users, *Surv. Geophys.,* **33**(1), 5–27.

Slezak, K., Jozwiak, W., Nowozynski, K., Orynski, S. & Brasse, H., 2019. 3-D studies of MT data in the Central Polish Basin: Influence of inversion parameters, model space and transfer function selection, *J. appl. Geophys.,* **161,** 26–36.

Sæmundsson, K., 1991. Geology of the Krafla system (in Icelandic), in *Náttúra Mývatns (The Natural History of Lake Mývatn),* The Icelandic Natural History Society Reykjavík, pp. 24–95.

ten Grotenhuis, S.M., Drury, M.R., Spiers, C.J. & Peach, C.J., 2005. Melt distribution in olivine rocks based on electrical conductivity measurements, *J. geophys. Res.,* **110**(B12), doi:10.1029/2004JB003462.

Tryggvason, E., 1994. Surface deformation at the Krafla volcano, North Iceland, 1982–1992, *Bull. Volcanol.,* **56**(2), 98–107.

Tryggvason, A., Rögnvaldsson, S.T. & Flóvenz, O.G., 2002. Three-dimensional imaging of the P-and S-wave velocity structure and earthquake locations beneath Southwest Iceland, *Geophys. J. Int.,* **151**(3), 848–866.

Ucok, H., Ershaghi, I. & Olhoeft, G.R., 1980. Electrical resistivity of geothermal brines, *J. Petrol. Tech.,* **32**(04), 717–727.

Usui, Y., Ogawa, Y., Aizawa, K., Kanda, W., Hashimoto, T., Koyama, T., Yamaya, Y. & Kagiyama, T., 2016. Three-dimensional resistivity structure of Asama Volcano revealed by data-space magnetotelluric inversion using unstructured tetrahedral elements, *Geophys. J. Int.,* **208**(3), 1359–1372.

Ussher, G., Harvey, C., Johnstone, R. & Anderson, E., 2000. Understanding the resistivities observed in geothermal systems, in *proceedings world geothermal congress,* Kyushu, Japan, pp. 1915–1920.

Watanabe, N., Numakura, T., Sakaguchi, K., Saishu, H., Okamoto, A., Ingebritsen, S.E. & Tsuchiya, N., 2017. Potentially exploitable supercritical geothermal resources in the ductile crust, *Nat. Geosci.,* **10**(2), 140–144.

Weisenberger, T.B. *et al.*, 2015. *Revision of the Conceptual Model of the Krafla Geothermal System.*In: ISOR Report to Landsvirkjun(unpublished).

Wolfe, C.J., Bjarnason, I.T., VanDecar, J.C. & Solomon, S.C., 1997. Seismic structure of the Iceland mantle plume, *Nature,* **385**(6613), 245–247.

Yang, B., Egbert, G.D., Kelbert, A. & Meqbel, N.M., 2015. Three-dimensional electrical resistivity of the north-central USA from EarthScope long period magnetotelluric data, *Earth planet. Sci. Lett.,* **422,** 87–93.

Yoshino, T., Laumonier, M., McIsaac, E. & Katsura, T., 2010. Electrical conductivity of basaltic and carbonatite melt-bearing peridotites at high pressures: Implications for melt distribution and melt fraction in the upper mantle, *Earth planet. Sci. Lett.,* **295**(3-4), 593–602.

Yoshino, T., 2018. Electrical conductivity measurement, in *Magmas Under Pressure,* pp. 281–319, eds Kono, Y. & Sanloup, C., Elsevier.

Zierenberg, R.A., Schiffman, P., Barfod, G.H., Lesher, C.E., Marks, N.E., Lowenstern, J.B. & Friðleifsson, G.Ó., 2013. Composition and origin of rhyolite melt intersected by drilling in the Krafla geothermal field, Iceland, *Contrib. Mineral. Petrol.,* **165**(2), 327–347.

The MathWorks, Inc., 2016. MATLAB and Statistical Toolbox Release 2016b, Natick, Massachusetts, United States.

Downloaded from https://academic.oup.com/gji/article/220/1/541/5587733 by guest on 30 March 2022

Appendix A

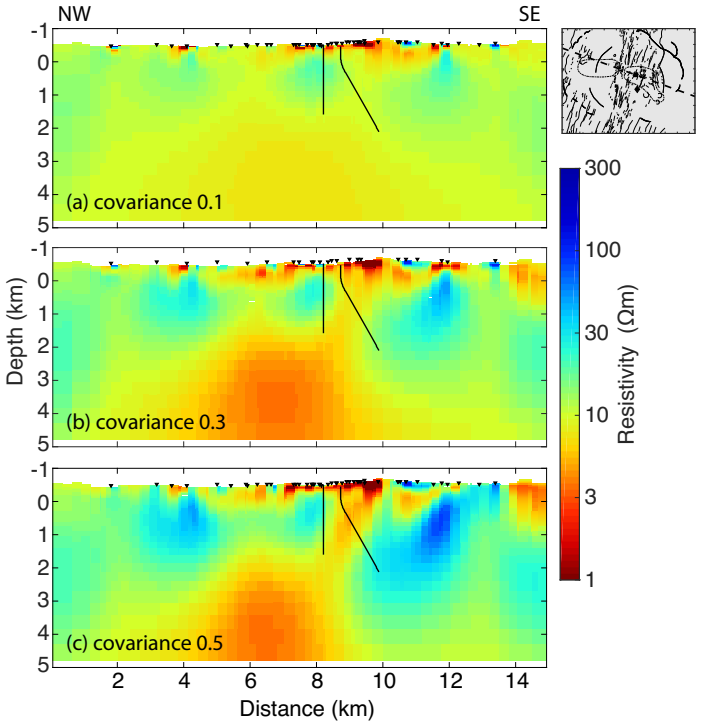

Figure A1. Diagonal slice through unconstrained inversion resistivity models with (a) model covariance setting 0.1 and r.m.s. misfit = 1.44 after 107 inversion iterations; (b) model covariance setting 0.3 and r.m.s. misfit = 1.04 after 98 iterations; (c) model covariance setting 0.5 and r.m.s. misfit = 1.19 after 66 iterations. See inset map for the profile trace.

Downloaded from https://academic.oup.com/gji/article/220/1/541/5587733 by guest on 30 March 2022